AN ABSTRACT OF THE THESIS OF

Colleen McKay Wall for the degree of Master of Science in Ocean, Earth and Atmospheric Sciences presented on January 14, 2014.

Title: Autonomous *in situ* Measurements of Estuarine Surface P_{CO_2}: Instrument Development and Initial Estuarine Observations.

Abstract approved:

_____

Burke R. Hales

A novel, low-cost instrument capable of measuring surface water P_{CO_2} was designed for use in dynamic, shallow-water environments. The instrument was tested in the Yaquina River Estuary, a macrotidal estuary known to experience a wide range of conditions ranging from dominance by the coastal ocean during summer upwelling to substantial freshwater discharge events resulting from winter storms. This instrument depends on gas equilibration by the diffusion of CO_2 molecules through a microporous, hydrophobic membrane between the aqueous environment and an enclosed gaseous volume, and subsequent quantification of the concentration of CO_2 molecules in the equilibrated air via Non-Dispersive Infra-Red (NDIR) absorbance technology. The field-testing occurred between January and December 2013, collecting over 200 discrete samples and 30 hours of *in situ* data. The data collected by this instrument was compared to discrete samples analyzed in the laboratory and found to have an absolute average deviation, or imprecision, of 7%. Preliminary area-weighted average air-sea CO_2 flux estimations for the Yaquina River Estuary (3 mol C m^{-2} y^{-1}) show the same order of magnitude as other estuarine studies where comparable P_{CO_2} measurement techniques were used, but significantly lower than studies

where P_{CO_2} was not directly measured. The discrete sampling program executed in combination with the instrument development process allowed a closer look at the seasonality of this ecosystem. This study discusses the evidence of both physical and biogeochemical processes occurring in the study area.

Autonomous *in situ* Measurements of Estuarine Surface P_{CO_2}: Instrument Development and Initial Estuarine Observations

by
Colleen McKay Wall

A THESIS

submitted to

Oregon State University

in partial fulfillment of
the requirements for the
degree of

Master of Science

Presented January 14, 2014
Commencement June 2014

Master of Science thesis of Colleen McKay Wall presented on January 14, 2014.

APPROVED:

Major Professor, representing Ocean, Earth, and Atmospheric Sciences

Dean of the College of Earth, Ocean, and Atmospheric Sciences

Dean of the Graduate School

I understand that my thesis will become part of the permanent collection of Oregon State University libraries. My signature below authorizes release of my thesis to any reader upon request.

Colleen McKay Wall, Author

ACKNOWLEDGEMENTS

I want to acknowledge the funding source for this research, NSF # OCE-CRI 1041267. My advisor Burke Hales has been a wonderful mentor, and friend for the past 3 years. A patient and thorough teacher who always took the time to ensure that I understood the concepts in depth and always managed to include his own sort of humor in every single meeting we had. This project would never have come together with the expertise of Dale Hubbard, whose generosity and friendship over the past 3 years I am grateful for. This research would not have been possible without help from other professional and amazing folks in various labs at CEOAS, namely Miguel Goni, Joe Jennings, Ben Russell, Jay Simpkins, Dave O'Gorman, Erik Arnesen, Dave Langner, Toby Martin, Daryl Swenson, Ann Swanson, Craig Risien, Mike Kriz, Jeff Crews, Walt Waldorf, and Danny Lockett. Thanks go to the Biogeochemical Earth class at CEOAS for the collection of data in Yaquina River Estuary referenced in this study. My graduate student friends were invaluable as sources of laughter, reflection, education, and reality-checks. Thank you so much for being there Elizabeth, Iria, Dave, Andrea, Caren, Jenny, Ale, Laurie, April, and Becky. My friends at my Reserve unit provided some breathing room from science. Thank you CAPT Somes and CDR Mattis for your guidance, mentorship, and cool-heads. Lastly and perhaps most importantly thank you to my wonderful family back in Virginia. Thank you to my amazing brother and sister, my two most favorite people in the whole world, for keeping me laughing and focused, and for quoting Jurassic Park with me as often as was necessary.

TABLE OF CONTENTS

TABLE OF CONTENTS (Continued)

LIST OF FIGURES

LIST OF TABLES

LIST OF APPENDIX TABLES

I. Introduction

1. The Global Carbon Cycle

As Earth's growing population continues to be dependent on fossil fuels as our primary source of energy, concerns grow about both the immediate and long-term effects of the steady rise in anthropogenic carbon dioxide (CO_2) output. While fossilized carbon cycling occurs over timescales of millions of years, anthropogenic CO_2 emissions to the atmosphere are subject to shorter cyclic timescales of only years to centuries (Sarmiento and Gruber 2006). In order to fully understand the current behavior of the world's oceans as a sink for anthropogenic carbon (Takahashi et al. 2002; Takahashi et al. 2009) due to the mounting effects of increased CO_2 release to the atmosphere, accurate and exhaustive measurements of carbon cycling between the atmosphere and global ocean are required.

1.1 Estuarine Observations

The broad range of environments classified as estuaries (Elliott and McLusky 2002) and the uncertainties of their physical and biogeochemical characteristics make it difficult to use measurements made in one location as a representation of biogeochemical processes in estuaries with significant geomorphological and hydrological differences (Cai 2011; Chen and Borges 2009; Evans et al. 2013; Crosswell et al. 2012). While the pelagic ocean is a known sink for anthropogenic carbon (Takahashi et al. 2002) the role of coastal estuaries is still largely uncertain, though some studies consider them to be

global sources of CO_2 to the atmosphere (Cai et al. 2000; Raymond et al. 2000; Borges 2005; Laruelle et al. 2010). These syntheses are dominated by studies of human-impacted estuaries of the Eurasian continent, and include few microtidal embayments (Crosswell et al. 2012) or upwelling environments like those on the Pacific coast of North America (Evans et al. 2013). The Chesapeake Bay, located on the Atlantic Coast of North America, has been classified as net autotrophic and therefore a CO_2 sink due to the large nutrient influx into this gigantic estuary, proving that estuaries must be understood individually before any classification of these unique ecosystems can be correctly made.

In upwelling dominated ocean margins, seasonal shifts in the wind direction cause upward movement of cold, salty, waters enriched with remineralized nutrients and CO_2 (Huyer 1977; Huyer et al. 1979; Hales et al. 2005). The upwelling dynamics of eastern boundary current systems (Carr 1998) coupled with the river-influenced estuaries rich with organic matter (Hatten et al. 2010) create unique ecosystems that are currently understudied.

It is estimated that the total estuarine derived CO_2 efflux may counteract 30% of the CO_2 absorbed from the atmosphere annually by the global ocean. This percentage is calculated from two well known estimates: 1) Borges (2005) global estuarine air-water CO_2 flux of 0.47 Pg C y^{-1} and 2) Takahashi et al. (2009) global ocean CO_2 absorption estimate of -1.6 Pg C y^{-1}. Estimates of the global estuarine efflux are calculated from air-sea CO_2 fluxes based on observation of the partial pressure of CO_2 (PCO_2) in the water that are determined in one of two ways: 1) *in situ* with a showerhead equilibrator (Broecker and

Takahashi 1966), a hydrophobic membrane contactor (Hales et al. 2004) or optical quantification with a pH-sensitive dye (DeGrandpre et al. 1995) or 2) by direct measurement of two of the three parameters Dissolved Inorganic Carbon (DIC), Total Alkalinity (T_{Alk}), or pH, and then calculating the PCO_2 based on thermodynamic relationships and mass and charge conservation.

The majority of estuarine carbonate chemistry studies use generalized laboratory techniques and sampling strategies (Frankignoulle et al. 1998; Cai and Wang 1998*)* designed for the open ocean where the extent of the biogeochemical processes are different than in an estuary. The temporal and spatial overlap of gas exchange, respiration, photosynthesis, and tidal and wind driven mixing, the close linkage between the estuary bed and the chemically complex water column are all factors that must be carefully considered when working in estuaries.

2. Carbonate Chemistry Dynamics

With few exceptions, estuarine air-water CO_2 flux (F, mmol m^{-2} d^{-1}) is calculated from surface PCO_2 using the following formula:

$$F = \gamma \times \left(k_w \times K_H \times \left(PCO_{2\,(water)} - PCO_{2\,(air)}\right)\right)$$

Equation 1

where k_w (cm h^{-1}) is the gas transfer velocity, K_H (mmol m^{-3} atm^{-1}) is the solubility constant, and $PCO_{2\,(water)}$ and $PCO_{2\,(air)}$ (atm) are the measured partial pressures of CO_2 in the water and atmosphere respectively. γ is a unit conversion constant given by:

$$\gamma = \frac{24\ h}{d} \times \frac{m}{100\ cm}$$

Equation 2

The gas transfer velocity is a factor driven by physical properties of the environment and will be discussed later. The atmospheric P_{CO_2} is relatively constant globally, and given the time periods of the data collection and the dynamic range of $P_{CO_{2\ (water)}}$, can be assumed constant at the global average. Variability in the $P_{CO_{2\ (water)}}$ is therefore the factor driving this estuarine CO_2 flux that we wish to constrain, and the specific component of the carbonate cycle studied in this research. The $P_{CO_{2\ (water)}}$ is related to the chemistry of the water by the equation:

$$PCO_{2\ (water)} = K_H \times [CO_{2\ (aq)}]$$

Equation 3

where $[CO_{2\ (aq)}]$ is the concentration of aqueous CO_2 molecules in the water and K_H (mmol m^{-3} atm^{-1}) is the solubility constant (Weiss 1974).

P_{CO_2} calculation techniques prove promising in the near constant-salinity open ocean where the most abundant sources of T_{Alk} are bicarbonate, carbonate, and borate (Broecker and Peng 1982; Sarmiento and Gruber 2006), and pH-dependence on salinity is minimized. In variable-salinity estuaries with a wide range of riverine chemical compositions these assumptions about T_{Alk} do not hold true (Hunt et al. 2011) and state-variable pH-dependences are large, therefore any calculation of P_{CO_2} based on them may be suspect. In order to determine any of these quantities, oceanographers utilize research vessels as a means to deploy sampling devices like CTD-rosette packages, towed bodies

such as the Lamont Pumping Sea Soar (Hales and Takahashi 2002), or deep-ocean and shelf-break moorings (Evans et al. 2011; Harris et al. 2013). These require large oceanographic research vessels that are not only costly to operate, but are limited in their capacity to operate in shallow waters of estuarine and nearshore settings.

3. Factors Driving P_{CO_2} Variability

Variability of oceanic P_{CO_2} is driven by alteration of both the chemical and physical properties of the water column (e.g. Broecker and Peng 1982; Emerson and Hedges 2008). Fluctuations in the T_{Alk} or the DIC (defined below) will drive changes in the speciation of the carbonate chemistry (Weiss 1974), altering the $[CO_{2\,(aq)}]$, and therefore, via Equation 3 above, the P_{CO_2}. The general formula for Total Alkalinity is defined as follows:

$$T_{Alk} = [HCO_3^-] + 2[CO_3^{2-}] + [OH^-] + [B(OH)_4^-] + [\Sigma_{wb}] - [H^+] - [\Sigma_{wa}]$$

Equation 4

where $[HCO_3^-]$ is the concentration of bicarbonate ion, $[CO_3^{2-}]$ is the concentration of carbonate ion, $[OH^-]$ is the concentration of hydroxide ion, $[H^+]$ is the concentration of hydrogen ion, $[B(OH)_4^-]$ is the concentration of borate ion, $[\Sigma_{wb}]$ is the sum of the concentrations of all weak bases in the system, and $[\Sigma_{wa}]$ is the sum of the concentrations of all weak acids in the system. The concentration of borate ($[B(OH)_4^-]$) is constrained by the fact that total boric acid concentration is conservative throughout the ocean, and determinable by simple proportion to salinity. *DIC,* also referred to in the literature as TCO_2 or ΣCO_2, is defined as:

$$DIC = \left[CO_{2\,(aq)}\right] + [HCO_3^-] + [CO_3^{2-}]$$

Equation 5

Variability in $[CO_{2\,(aq)}]$ is driven by the total abundance of carbon in the water and the portion of that total existing in the form of $[CO_{2\,(aq)}]$, which is driven by changes in the acid-base balance. The shifts in acid-base equilibrium are very rapid, resulting in a system that is nearly always at thermodynamic equilibrium.

The drivers for changing the T_{Alk} : DIC, thereby causing rapid shifts in equilibrium speciation, are biogeochemical processes, specifically photosynthesis, respiration, calcium carbonate ($CaCO_3$) precipitation and $CaCO_3$ dissolution (Feely et al. 2004). The Redfield-Ketchum-Richards (RKR) ratio, which states that the majority of ocean biota have a ratio of carbon to nitrogen to phosphorus of 106:16:1 (Redfield 1934), determines how the T_{Alk} : DIC will vary based on certain biogeochemical processes. Photosynthesis removes both DIC and nutrients from the water column. The removal of macronutrients, namely nitrate (NO_3^-) and phosphate (PO_4^{3-}), increases the T_{Alk} due to a decrease in the concentration of free protons. The RKR of ΔDIC: ΔT_{alk} is -106:16 for photosynthesis, such that the large decrease in DIC is augmented by the small increase in T_{Alk}, and therefore there is an overall decrease in the $[CO_{2\,(aq)}]$.

Calcifying organisms play a large role in the carbonate chemistry cycle of the ocean as well (Wilbur and Saleuddin 1983; Milliman 1993; Lebrato et al. 2010). These organisms precipitate $CaCO_3$ to form their protective structures during life, and after death, these structures can dissolve. In the case of large bivalves, the components are returned to the water column with average half-

lives of 2 to 10 years (Powell et al. 2006). $CaCO_3$ dissolution increases both T_{Alk} and DIC, (in a 2:1 ratio respectively) with the increase in T_{Alk} dominating the reaction and driving $[CO_{2\,(aq)}]$ down (Broecker and Peng 1982; Zeebe 2012). The opposite is true for $CaCO_3$ precipitation.

Gas exchange occurs only at the water surface that is in direct contact with the atmosphere, although its signature can be mixed to greater depths. From Equation 4 for T_{Alk} and Equation 5 for DIC, only the latter includes a component that is affected by gas exchange, $CO_{2(aq)}$. Gas exchange thus changes DIC, while having no effect on T_{Alk}.

4. Unique Aspects of Estuaries

In estuaries, the concept of T_{Alk} becomes more complex due to the addition of non-carbonate-based allochthonous organic acids and their conjugate bases (Hunt et al. 2011) that are transported into rivers and streams via overland runoff, groundwater, or horizontal movement from adjacent salt marshes (Cai et al. 1998). The presence of these complex organic acids shifts the dominance of the T_{Alk} signal away from the carbonate species and toward the weak acids. This poses a problem when attempting to interpret measurements of T_{Alk} performed in a laboratory setting using titration methods.

In most cases, estuaries are areas where freshwater and saltwater masses mix (Pritchard 1967). Conservative mixing of fresh and saltwater sources results in linear dependence of T_{Alk} and DIC on salinity; consumption or production within the environment by the processes listed above can be seen as

negative or positive departures from the conservative mixing line. Freshwater input to estuaries varies seasonally in most temperate zones, where winter rainstorms cause large influxes of organic material and freshwater from the small mountainous river systems (SMRS) (Hatten et al. 2010). In summer and early fall, the freshwater input is very low and during this time the estuary experiences higher oceanic influences.

The rate of gas exchange for a given degree of air-sea unsaturation in the open ocean is a result of wind-driven mixing; however, in an estuary, tides and bed friction create a more dynamic environment for mixing (Alin et al. 2011; Raymond and Cole 2001). The estuary bed varies in depth and texture over the extent of an individual basin, and the flow over the bed varies with river discharge and tidal phase. The semi-diurnal tidal regime that is present on the Pacific coast of North America, such as in the Yaquina River Estuary (YRE), causes this basin to experience two high and two low tides daily with an average tidal amplitude of 2.4 m (McIntire and Overton 1971).

Respiration and photosynthesis occur with an intensity in estuaries that is driven by many factors such as the light availability or depth of the euphotic zone, nutrient content, coupling with the benthic zone (Koseff et al. 1993), and seasonal variability in biogeochemical processes (Green et al. 2006). The benthic zone of an estuary could include mudflats (areas of increased anaerobic metabolism), seagrass beds (areas of increased photosynthesis and respiration), and shellfish communities ($CaCO_3$ dissolution and production regions), with which the brackish waters interact (Callender and Hammond 1982). Fluctuations

in the concentrations of the carbonate system constituents driven by the processes above make current sampling methods limited in their representation of the entire estuarine system, as their resolution is not sufficient to capture such potentially dynamic changes.

II. Autonomous Coastal Drifting CO_2 System Development and Testing

1. Purpose

While analysis of the carbonate system of the pelagic ocean has become standard over the past two decades by methods such as coulometric titrations (Millero et al. 1993), gas equilibration (Hales et al. 2004), acid titration (Edmond 1970), and potentiometric measurements (Takahashi et al. 1970), the analysis of estuarine waters is inconsistent and incomplete. Our objective, therefore, was to develop a system to measure the P_{CO_2} of the surface estuarine waters with a response time fast enough to capture the potentially rapid changes in P_{CO_2} driven at tidal to diel timescales. Salinity, water temperature, and location were required for carbonate chemistry calculations and physical perspective. I aimed to ensure that the *in situ* data points were highly correlated with other well-documented techniques for measuring P_{CO_2}.

This research consisted of the development of and initial field data collection with an Autonomous Coastal Drifting CO_2 (ACDC) instrument, and our attempts to understand the physical and biogeochemical influences on the P_{CO_2} signal. In order for the acquired data to be of scientific value, this system had to be sufficiently accurate, stable, and responsive to the dynamic range expected in

estuarine and near-shore aquatic ecosystems. The system needed to be small in size to allow for flexible deployment strategies from any sort of research platform. It was also essential that this platform be a low cost unit that is both trackable and self-reporting as the tempestuous nature of these environments could make recovery impossible, forcing a reliance on its self-reporting capabilities to a base station computer.

In order for the ACDC system to yield useful data in the desired environment, it must first meet several specific requirements. This instrument must have sufficient accuracy and precision in all of its metrics (i.e. P_{CO_2}, salinity, water temperature, and location) to be comparable to known equilibrated-head-space P_{CO_2} determinations, and have a response time comparable to that of other *in situ* P_{CO_2} instruments, such as the SAMI-CO_2 (Submersible Autonomous Moored Instrument for CO_2) produced by Sunburst Sensors, LLC (DeGrandpre et al. 1995). Water temperature measurements were necessary as they have a direct impact on CO_2 gas solubility as discussed above (Equation 3). A measurement of salinity is necessary for two reasons: 1) to understand the mixing dynamics between the fresh water of the river and saltwater of the ocean within an estuary and 2) along with temperature, for estimation of the various carbonate species in the water. All of the sensors chosen to operate aboard the platform must show stable and identifiable relationships between the environmental signal and the raw sensor output. The dynamic range of all sensors must encompass expected conditions within the desired testing environments. For instance, the CO_2 sensor I chose has a range of 0-10,000

ppm; discrete sampling of the freshwater and ocean end members of the YRE show a range of 60-1200 µatm for P_{CO_2}, well within the chosen sensor's capabilities. The instrument response time (τ) must be comparable to other *in situ* CO_2 instruments such as the SAMI which has a response time of 5 minutes (DeGrandpre et al. 1995). When selecting components for this platform, I specifically selected sensors with both the lowest operating and quiescent current draw, in order to prolong operational endurance of this battery powered instrument. Lastly, I needed the ACDC to be trackable and self-reporting in order to 1) retrieve continuously collected data from the sensor, 2) locate the sensor at the end of its scheduled deployment, and 3) safeguard security of historical data at a base station computer if the sensor is unrecoverable.

Here, I present the theory and technical specifications for the ACDC as well as the first autonomous *in situ* P_{CO_2} data collected from field sites on the Oregon coast taken from both Eulerian and Lagrangian sampling strategies. The field-testing occurred in Newport, OR in the YRE, a 13 km^2 macrotidal estuary (Quinn et al. 1991) experiencing the effects of seasonal upwelling in the local coastal ocean, and fed by the Yaquina River. This research, devoted to further refining this platform, will lead to improved data collection methodology, and seeks to offer data that will help constrain the estuarine carbon cycle and allow for improved predictions regarding ocean acidification and the effects of anthropogenic carbon emissions.

2. Principles of Operation

The ACDC system depends on gas equilibration by the diffusion of aqueous CO_2 molecules through a microporous, hydrophobic membrane between the aqueous environment and an enclosed gaseous volume, and subsequent quantification of the concentration of CO_2 molecules in the equilibrated air.

2.1 Molecular Diffusion Basics

Fick's Law describes the rate of molecular diffusion,

$$J = D \times \frac{\delta C}{\delta x}$$

Equation 6

where *J* is the diffusive flux (i.e. concentration area^{-1} time^{-1}), *D* is the diffusivity of CO_2 in air (i.e. area time^{-1}), and $\frac{\delta C}{\delta x}$ is the concentration gradient between the CO_2 molecules outside the equilibrator versus those inside the equilibrator.

2.2 Non-Dispersive Infrared Basics

The K-30 CO_2 sensor (www.co2meter.com, #SE-0018) chosen as the heart of the ACDC system employs non-dispersive infrared (NDIR) technology (Goody 1968) for gaseous CO_2 detection. An NDIR detector functions by sending light from a source through a sample chamber and filtering for a wavelength specific to the gas of interest. From Beer's law it is understood that light intensity measured at the detector (I_C) is related to source intensity (I_0), and the absorption (*A*) by the following equation:

$$I_C = I_0 \times 10^{-A}$$

Equation 7

Absorption is proportional to concentration (*C*):

$$A = \varepsilon l C$$

$$C = -(\varepsilon l)^{-1} \times \log\left(\frac{I_C}{I_0}\right)$$

Equation 8

where ε is the molar absorptivity constant (concentration^{-1} length $^{-1}$) and l is the pathlength between source and detector. By measuring the difference in light intensity from the source to the detector, the sensor determines absorbance at a wavelength characteristic of CO_2, and from that, the number of CO_2 molecules in the detection pathway can be determined.

3. System Description and Operation

I have designed an autonomous drifting PCO_2 system based on gas equilibration through a hydrophobic microporous membrane and subsequent measurement of CO_2 content of the equilibrated gas volume using NDIR absorbance. During each deployment of this new platform, I collected discrete check samples throughout the day to verify proper operation and calibration of the instrument. *In situ* data was collected during October – December 2013.

3.1 System Component Descriptions

3.1.1 Gas Equilibrator

The ACDC system uses a uniquely designed gas equilibrator to provide a gaseous volume that is thermodynamically linked to the ambient CO_2 chemistry via Equation 3, above. The equilibrator consists of a hydrophobic microporous sheet membrane (described below) wrapped around a perforated cylindrical 304-alloy stainless steel support frame (http://perforatedtubes.com). The support frame measures 1 inch in diameter by 4 inches in length. Perforations were 1/16" diameter in a staggered pattern resulting in 40% open area of the frame. A 304-alloy stainless steel 3/4" NPT (National Pipe Taper) threaded nipple was welded onto one end of the support frame and a blank 304-alloy stainless steel plug into the other end.

The hydrophobic microporous membrane consists of Celgard® 2400 (http://www.celgard.com). This material is a highly hydrophobic polypropylene sheet with a thickness of 25 μm, a porosity of 41% and an average pore size diameter of 0.043 μm. The hydrophobicity and small pore diameter of the material effectively block transgression of liquid water, but allow gases to move freely across the membrane. Celgard® donated samples for academic use to our laboratory.

The material was cut to match the size of the perforated tube support. The perimeter of the membrane was coated in Sylgard® 184 silicone elastomer (www.dowcorning.com) at a width of about 1/4", and allowed to dry in a 50°C oven overnight. The prepared membrane was then wrapped around the support tube, adhered with marine grade silicone sealant at the treated edges, and

allowed to dry overnight to achieve a full watertight seal. Figure 1 is a diagram of the custom designed equilibrator.

3.1.2 Gas-phase CO_2 Detector

CO_2 in the equilibrated gas phase is detected via NDIR absorption with a K-30 sensor (www.co2meter.com), which has a detection range of 0-10,000 ppm. This small (51 x 57 x 14 mm), inexpensive ($65.00 USD) sensor measures the number density of CO_2 molecules in its optical detection pathway. The K-30 was designed as an open-air detector, and as a result has no sealed detector volume. To maintain the integrity of the detector-equilibrator loop, a machined, sealed aluminum block was built to house the sensor, connected to the 1/8” ethylene tetrafluoroethylene (EFTE) tubing linking the detector and equilibrator volumes. I use the sensor’s digital MODBUS serial output for the CO_2 signal, though it does have scalable analog outputs as well.

3.1.3 Additional Recirculation Loop Components

The gas stream is recirculated between the equilibrator via a closed loop with a Hargraves-Fluidics micro-air pump (www.hargravesfluidics.com, #E134-11-050), which provides a flow rate of approximately 0.5 L min^{-1}. After exiting the equilibrator, the gas stream first passes through a hydrophobic filter (www.balstonfilters.com, #9922-11) to remove liquids and aerosols from the air stream in order to protect the electronic components downstream. The gas stream then passes through the pump and into the housing for the K-30 sensor. Upon exiting the sensor housing, the air stream passes by a barometric-range

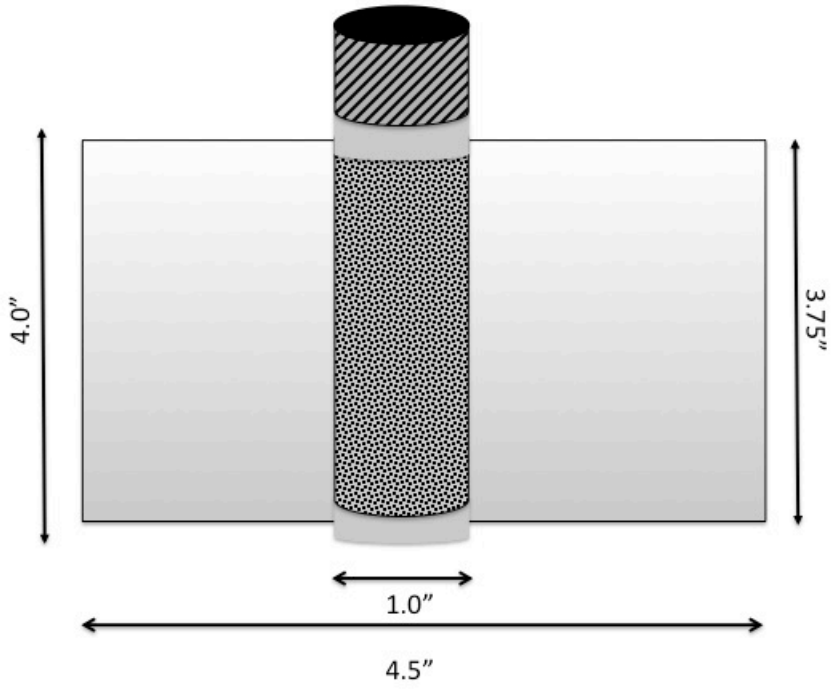

Figure 1: Equilibrator Schematic. Approximate dimensions of membrane (4.5” x 3.75”) and equilibrator (4.0” long, 1.0” diameter). Threaded pipe nipple end is shown with diagonal striping. The perforated holes of the equilibrator frame are shown as patterned dots.

pressure sensor (www.digikey.com, #BARO-A-4V-MINI) used to measure total loop pressure, before reentering the equilibrator again and closing the loop. Figure 2 is a schematic of the recirculating gas loop. With a total system volume of approximately 61 mL (including the equilibrator), the flushing time for the loop is approximately 8 seconds. I also monitor the temperature of the internal instrument environment with a DS18B20 digital surface temperature sensor (www.adafruit.com, #374).

3.1.4 Ancillary Sensor Measurements

In addition to measuring P_{CO_2} and monitoring the internal conditions of the instrument housing, the system measures the temperature and conductivity of the ambient surface waters. On either side of the equilibrator on the bottom of the instrument housing, a watertight pass-through fitting allows for the exposure of one of two sensor probes. The DS18B20 digital water temperature probe (www.adafruit.com, #381) provides a temperature reading utilizing OneWire protocols and is connected in series with the internal temperature sensor. Each DS18B20 has its own unique address, and is polled in turn for temperature measurements. A conductivity driver and amplification circuit produced by NW Metasystems, Inc., and a probe constructed in our laboratory are used to measure conductivity. Powered directly from the battery pack, this probe provides an analog output (mV) inversely proportional to the conductivity of the water. A calibration curve is created from the calculated values of conductivity of dilution-series of 35 practical salinity unit (psu) standard seawater and the inverse of the probe's mV output with a log-log regression. During post-data

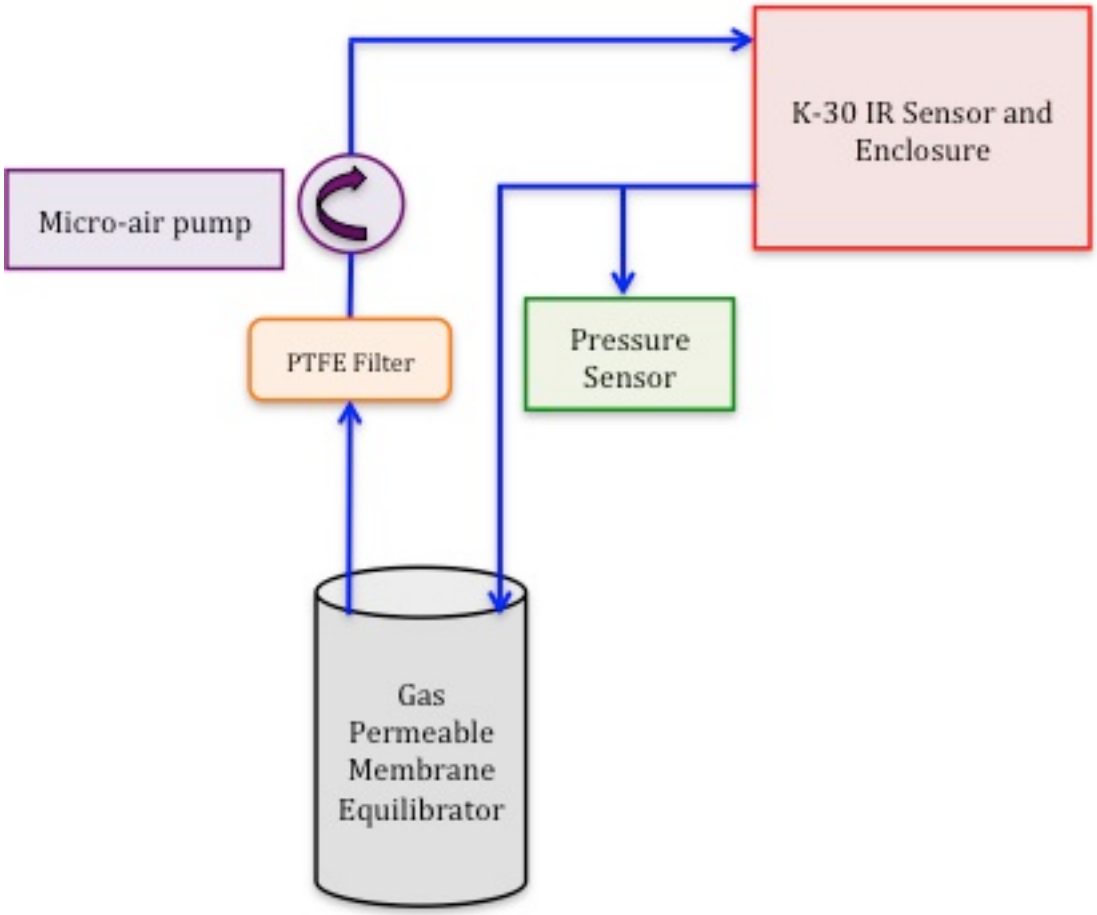

Figure 2: Schematic of the P_{CO_2} recirculation loop. The equilibrated gas sample line is pumped from the equilibrator through the hydrophobic polytetrafluoroethylene (PTFE) filter past the pump and into the K-30 NDIR enclosure at approximately 0.5 L min^{-1}. Gas leaves the sensor housing flowing past a barometric pressure sensor and back into the equilibrator.

analysis I determine salinity by utilizing the measured water temperature and conductivity values in accordance with the well-known relationships of Perkin and Lewis (1980). A Garmin LVC 18x (www.garmin.com, 010-00321-31) Global Positioning System (GPS) unit reports the instrument position. The GPS reported the “GLL”, or geographic latitude and longitude NMEA sentence containing the latitude, longitude, and a Coordinated Universal Time (UTC) timestamp when the GPS fix was taken, as well as other values not relevant to this research.

3.1.5 System Control, Logging, Telemetry, and Tracking

I chose an Arduino Mega 2560 R3 (www.arduino.cc, A000067) as the microcontroller to drive the data collection and overall system operation. Figure 3 is a schematic of the various sensors’ connections with the Arduino. Arduino micro-controllers are open-source electronics platforms with basic functionality that can be increased by adding mate-able circuit boards, or “shields” to the base microcontroller. I employed the Arduino GSM Shield for cellular communications, and the Adafruit Datalogger Shield for Real-Time-Clock and data storage via Secure Digital (SD) card functionality. The deployment code is written in the Arduino IDE environment based on the C++ language. A copy of the code used for deployments is included in Appendix B. The Arduino Mega 2560 R3 is powered by a battery pack producing 8.6V that is regulated to 5V by the microcontroller itself. This 5V is used to power the Garmin LVC 18x GPS, K-30 CO_2 sensor, Allsensors Pressure Sensor, and Hargraves Fluidics micro-air pump. The battery pack is used to directly power the conductivity board from the

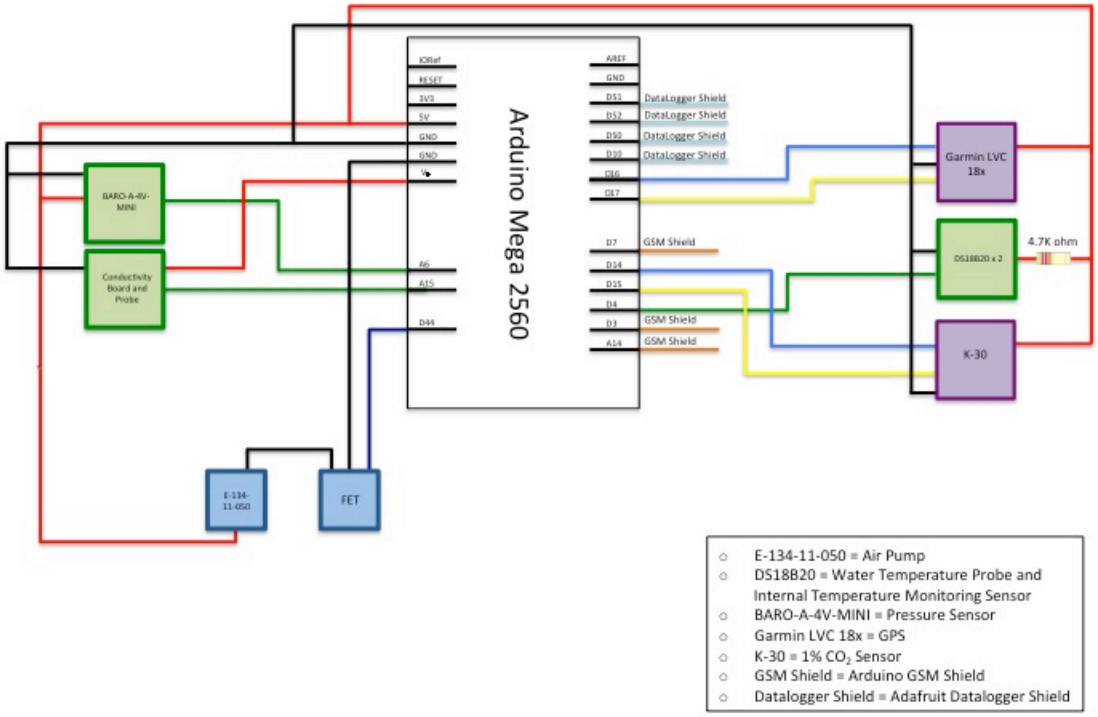

Figure 3: Schematic of the Arduino Mega 2560 and all connections to auxiliary sensors and components. The key at the bottom right describes the purpose of each component. Power wires are shown in red, ground wires are shown in black. A colored line extending from the pin listing the shield usage annotates pins that are dedicated to a stackable shield.

V_{IN} port on the Arduino Mega 2560 R3. I used the Arduino Mega's digital I/O terminals to drive one field effect transistor (FET) (www.digikey.com, #RFP12N10L-ND) circuit to switch the state of the micro-air pump. The platform becomes self-reporting and trackable by utilizing GSM/GPRS technology, also known as 2G cellular. The modem shield allows recently collected data to be sent via text message to a designated phone number. This would allow access for monitoring the system location while in the field via smart phone and from the laboratory at a computer connected to the Internet. While my research was not successful in fully integrating the GSM cellular shield into the larger system, in the future, I expect all data fields will be sent via cellular modem for processing and analysis at the base station computer.

4. Laboratory Performance and Calibration Procedures

4.1 K-30 CO_2 Detector Calibrations

4.1.1 Dry-Gas Standard Calibrations

Manufacturer's specifications for the accuracy and repeatability of the K-30 sensor are $\pm$ 30 ppm $\pm$ 3% of measured value and $\pm$ 20 ppm $\pm$ 1% of measured value respectively. These values are functional for the estuarine environment where published dynamic ranges in P_{CO_2} exceed 1000s of µatm, however, I wanted to verify these specifications and determine if a more rigorous calibration would yield any improvement. The K-30 sensor was calibrated in the laboratory before and after each deployment. I used gas standards analyzed in T. Takahashi's laboratory at the Lamont Doherty Earth Observatory (LDEO) with

known mixing ratio (XCO_2) values of 407.21, 1001.5, 1515.0, and 2975.0 ppm, with the balance being dry Ultra Pure Air (UPA). Since the K-30 sensor appears to respond to PCO_2 rather than XCO_2 (see below), I converted the known cylinder mixing ratios to μatm by multiplying by the pressure measured by the loop sensor in the system. Figure 4a shows a gas standard calibration curve for the K-30 sensor. I tested the K-30 sensor for calibration stability by performing these laboratory calibration procedures before and after deployments and plotting the slope and intercept of each calibration, as shown in Figure 4b. The change in the slope is based on the initial calibration slope determined on 6-Feb-13. The relative average deviations of the slope and R^2 values are found to be 1.3% and 0.01%, respectively. The average absolute deviation of the PCO_2 value predicted from the raw K-30 signal from the LDEO standards is 0.6%. This result suggests that the K-30 sensor, when individually calibrated with quality gas standards, is capable of achieving stability and accuracy that exceeds the manufacturer's specifications.

4.1.2 Temperature, Pressure, and Humidity Sensitivity

The K-30 sensor is designed for ambient-air CO_2 detection, and published specifications claim temperature compensation and state nothing regarding humidity and ambient pressure sensitivity. These effects may be minor in the intended sensing environment and within the stated performance of the sensor, but the estuarine environment is likely to be variable and the calibration tests described above showed that detector performance could be affected by these environmental conditions. I tested the detector's response to varying temperature

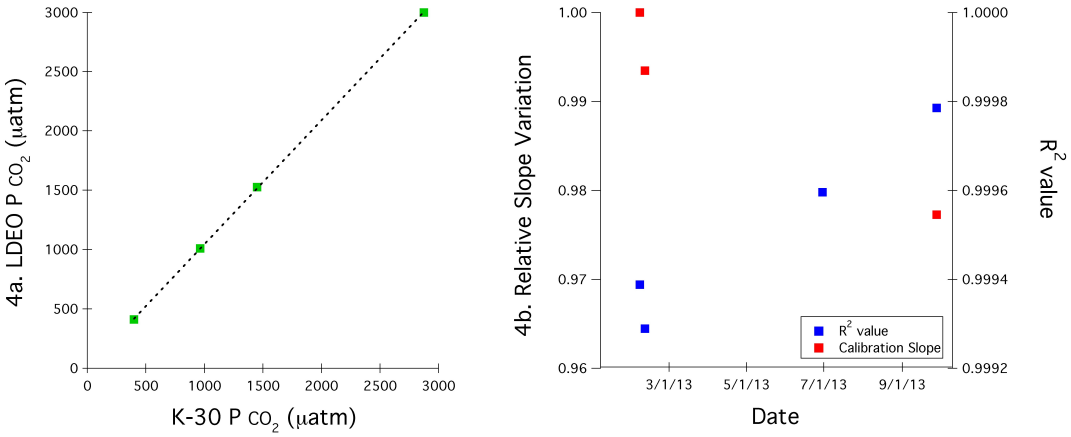

Figure 4: Laboratory gas calibration curve results for a K-30 PCO_2 sensor. Figure 4a: PCO_2 obtained from the K-30 NDIR detector versus gas standard PCO_2 from LDEO certified gas standards converted to µatm using the measured pressure from the loop pressure sensor in atm. Figure 4b: Time series plots of relative slope variation (red squares on left axis) and R^2 (blue squares on right axis) of LDEO gas standards versus K-30 measurement.

from 1°C to 20°C, and found no significant change in signal for the known PCO_2 values of our calibration range. By restricting flow from a certified standard gas cylinder and recording the K-30 signal and the system pressure with the integrated sensor, I found that the K-30 signal for a fixed XCO_2 gas mixture increased proportionally to the increase in total pressure. The K-30 sensor thus detects the partial pressure of the gas, rather than its mixing ratio.

While the K-30 is calibrated in the laboratory with dry certified gases, when deployed, the internal gas loop of the instrument operates at approximately 100% humidity with respect to the temperature of the ambient water. I used dry, CO_2-free ultra-pure air (UPA) bubbled through fresh deionized (DI) water to achieve a 100% humidity air stream in the laboratory. I then varied the temperature of the DI water and allowed the temperature to first drop and then warm back to room temperature while recording water temperature and K-30 signal. I calculated the vapor pressure of water from the measured water temperature based on data and equations from Ambrose and Lawrenson (1972). From these calculated vapor pressures, I empirically determined a linear relationship between the K-30 sensor output and vapor pressure, resulting in a correction to the raw K-30 signal. I then applied the dry-gas-standard calibration curve from above to the humidity corrected signal to determine the portion of the K-30 signal derived from CO_2 molecules in the gas stream. Calibration curve equations are as follows:

$$V_{H_2O} = 6\times10^{-5}(T^3) + 5\times10^{-4}(T^2) + 0.055T + 0.571$$

$$K30_{(H_2O)} = m_{(H_2O)}\left(V_{H_2O}\right) + b_{(H_2O)}$$

$$K30_{(CO_2)} = \left[\left(K30_{(raw)} - K30_{(H_2O)}\right) \times m_{(dry)}\right] + b_{(residual)}$$

Equation 9

where V_{H_2O} is the vapor pressure of water (kPa), T is the water temperature (^oC), $K30_{(H_2O)}$ is the portion of the K-30 signal due to the presence of water vapor, $m_{(H_2O)}$ and $b_{(H_2O)}$ are the slope and intercept of the K-30 signal vs. vapor pressure linear regression, $K30_{(CO_2)}$ is the portion of the K-30 signal due to the presence of CO_2, $K30_{(raw)}$ is the raw K-30 output, and $m_{(dry)}$ and $b_{(residual)}$ are the slope and intercept of the dry-gas calibration curves. The slope and intercepts for a zeroed and spanned K-30 sensor were found to be of order 8 for $m_{(H_2O)}$, 10 for $b_{(H_2O)}$, and 1 for $m_{(dry)}$. The constant term in the sensor water vapor dependence includes the raw detector blank, and its subtraction from the K-30 CO_2 dependence accounts for that correction. The CO_2 dependence shown above resulted from a regression that allowed a non-zero intercept, but the blank correction in the water-vapor term and small value of this intercept ($b_{(residual)}$) suggest it is probably not significantly different from zero. Once properly calibrated and compensated, I believe the overall accuracy of the K-30 sensor far exceeds that advertised by the manufacturer and is ideally suited for our purposes.

4.2 Response Time

The need for a fast response time in a dynamic environment is undeniable in order to fully resolve the variability of surface PCO_2 as a faster response time allows visualization of the high resolution changes expected in the surface

estuarine waters. To this end, I measured the response to sudden changes in ambient gas and liquid PCO_2. Because the ambient gaseous environment is difficult to control, I opted to flush the detector/equilibrator loop with widely varying gas compositions, and then monitored the subsequent response to either ambient outside air (for gas-phase determinations) or a volume of well-mixed water sourced from the YRE (for liquid-phase determinations).

4.2.1 Response Time Methods

Gas-phase response time experiments were conducted using cylinders of compressed UPA and then repeated with a 980 ppm XCO_2 gas standard. The standard gas was allowed to flow through the system's open recirculating air loop until the K-30 sensor reading had stabilized at the appropriate value. A three-way valve was then switched shutting off the flow of gas, and closing the circulation loop. The micro-air pump was then turned on and data recorded as the system responded. Data was collected until the K-30 sensor reading had stabilized back to atmospheric values of PCO_2. Liquid phase response time was determined in a similar manner. To measure the response time of the system to a step change in PCO_2 of a liquid, the equilibrator was flushed with UPA and submerged in a covered container full of seawater taken from Yaquina Bay, OR. The liquid response time was not repeated using the high gas standard due to the relatively high value of PCO_2 in our sample seawater. A bilge pump (Rule, #RUL-PMP-24) continuously stirred this container. With the equilibrator submerged, UPA was pumped through the loop until the detector PCO_2 reading reached a stable value. The flow of UPA was then disconnected and the closed sample loop reset. The

micro-air pump was then started, and run continuously until the PCO_2 reading stabilized to a value equivalent to that of the water in the container as verified by a check sample analyzed with techniques as used by Barton et al. (2012).

4.2.2 Response Time Model and Calculations

Figures 5a and 5b are plots of the gas-phase and liquid-phase response time data along with modeled predictions of a first-order response to a step change in ambient signal. The modeled data is generated from the following equation:

$$PCO_{2\,(t)} = PCO_{2\,(0)} + \Delta PCO_2 \left(1 - e^{-\alpha t}\right)$$

Equation 10

where $PCO_{2\,(t)}$ is the PCO_2 at a given time *t*, $PCO_{2\,(0)}$ is the initial PCO_2 value, t is the elapsed time in minutes since the initiation of the step change, and ΔPCO_2 is the difference between the final and initial internal PCO_2.

If we assume that the detector response time is fast, that the ambient environment is infinite and well-mixed all the way to the equilibrator surface, and that the interior volume of the PCO_2 sensor housing is also well mixed, then the response time of the sensor can be estimated by the total transport of CO_2 across the membrane divided by the total CO_2 reservoir within the detector-equilibrator loop:

$$\frac{1}{\tau} = \frac{A_{exch} \times J}{V_{sys} \times C}$$

Equation 11

where *J* is the diffusive flux (Equation 6), A_{exch} is the area over which gas exchange occurs, V_{sys} is the total volume of the equilibrator-detector loop, and *C*

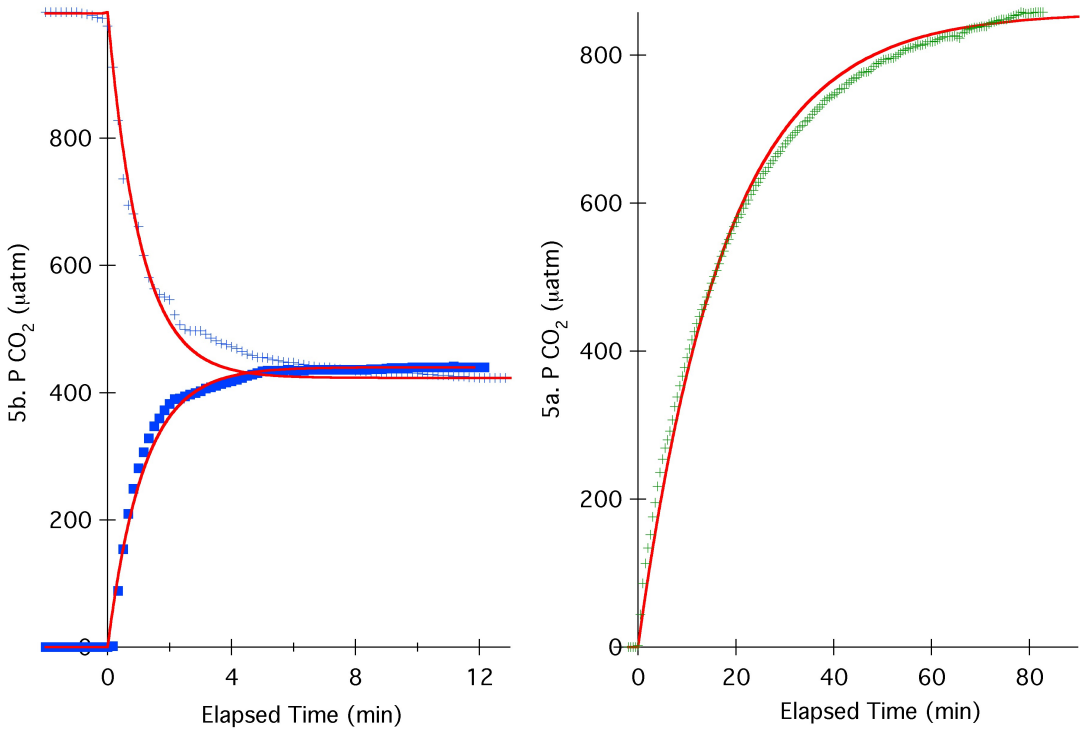

Figure 5: Response Time Plots. Figure 5a: Gas Phase Response Time: Blue data points are from the bench-top testing using calibrated standard gases to flush the plumbing loop. Figure 5b: Liquid Phase Response Time: Green data points are from the bench-top testing using UPA to flush the plumbing loop. The red line is the modeled data.

is the concentration of CO_2 in the equilibrator-detector loop. When Equation 6 is substituted into Equation 11 for *J*, the final relationship between the physical properties of the gas equilibration loop and the response time is Equation 12:

$$\frac{1}{\tau} = \alpha = \frac{D_{eff} \times A_{exch}}{V_{sys} \times T_{mem}}$$

Equation 12

where D_{eff} is the effective diffusivity ($cm^2\ s^{-1}$) and T_{mem} is the membrane thickness (cm) or diffusive pathlength. I calculated values of 16 cm^2 for A_{exch}, 61 cm^3 for V_{sys}, and 0.0025 cm for T_{mem}, based on the known physical dimensions of the system and the characteristics of the membrane.

For gas-phase testing a response time of 1.1 minutes is calculated from the model (Equation 10). From the time-constant determined by fitting the experimental data to the model curve, I calculate an effective cross-membrane diffusivity of 1.5 x 10^{-4} $cm^2\ s^{-1}$. For liquid-phase testing, a response time of 17.9 minutes is calculated from the model. Fitting the experimental data to the model here results in an effective diffusivity of 9.0 x 10^{-6} $cm^2\ s^{-1}$.

The difference these measured diffusivities (Table 1) compared to documented values (Cussler 2009) points to a fundamental misunderstanding of the characteristics, dynamics, and performance of the system.

	Diffusivity ($cm^2\ s^{-1}$)	
Phase	Experimental	Literature
Gas	0.00015	0.16
Liquid	0.000009	0.000016

Table 1: Experimental and Literature Diffusivities

explanation for this. The pathway across the membrane is not necessarily equivalent to the T_{mem} from Equation 12; tortuosity in the diffusive path might actually serve to increase the effective thickness of the membrane. Since the diffusive time constant increases quadratically with the diffusive path length, this might have amplified effects on the response time. Still, even assuming an effective doubling of the diffusive path length and a halving of the exchangeable area leads to estimation of an effective cross-membrane diffusivity that is over 100 times slower than the known diffusivity of CO_2 in air.

The over 15-fold slower response time in water is additionally confusing. The characteristics of the equilibrator are unchanged, so this must mean that there is an additional barrier to diffusive transport in the aqueous medium. This is possibly the result of an aqueous diffusive sub-layer around the equilibrator. Although even such considerations initially seemed unlikely, there was a definite and significant change in the experimental response time as the mixing rate in the test reservoir was increased. Using a lower-flow aquarium pump led to response almost 1.5 times longer, while performing the tests with no mixing result in response times of 2.3 hours. This is an important consideration for field experiment design, as more quiescent environments will lead to slower instrument response.

5. Field Performance

5.1 Validation Sample Comparison

Fixed-location deployments occurred over a period of approximately 6 hours during ebbing tides. During each deployment, whether the system was moored or drifting freely, discrete check samples were taken every 15 to 20 minutes to establish the accuracy of the platform. Clean 350 mL amber glass bottles were first rinsed with ambient water three times, and then filled with water from approximately 50 cm below the surface leaving 3 mL of headspace in the top of the bottle. The GPS position of the discrete sample (when possible) and water temperature were recorded, and the sample preserved with 30 μL of saturated mercuric chloride ($HgCl_2$) solution before sealing with crimp-seal urethane-lined metal caps. The amount of $HgCl_2$ added was minimized to reduce the acidic effects of this preservative in weakly buffered low-salinity estuarine water (Swanson and Hales, unpubl). These samples were analyzed for P_{CO_2} and DIC using methods from Barton et al. (2012). Figure 6 is a plot of *in situ* P_{CO_2} obtained by ACDC vs. discrete bottle P_{CO_2}. The red data points have been humidity corrected and calibrated using the dry-gas standard calibration curve described above (Equation 9). The blue data points have additionally been corrected using an empirically determined factor due to the difference in true atmospheric P_{CO_2} (~ 400 μatm) and that measured at the start of each deployment cycle. Despite our best efforts to properly calibrate the K-30 sensor, there remains an offset from the known value of atmospheric P_{CO_2} when the sensor is in the field. Equation 13 is used to calculate the average relative deviations:

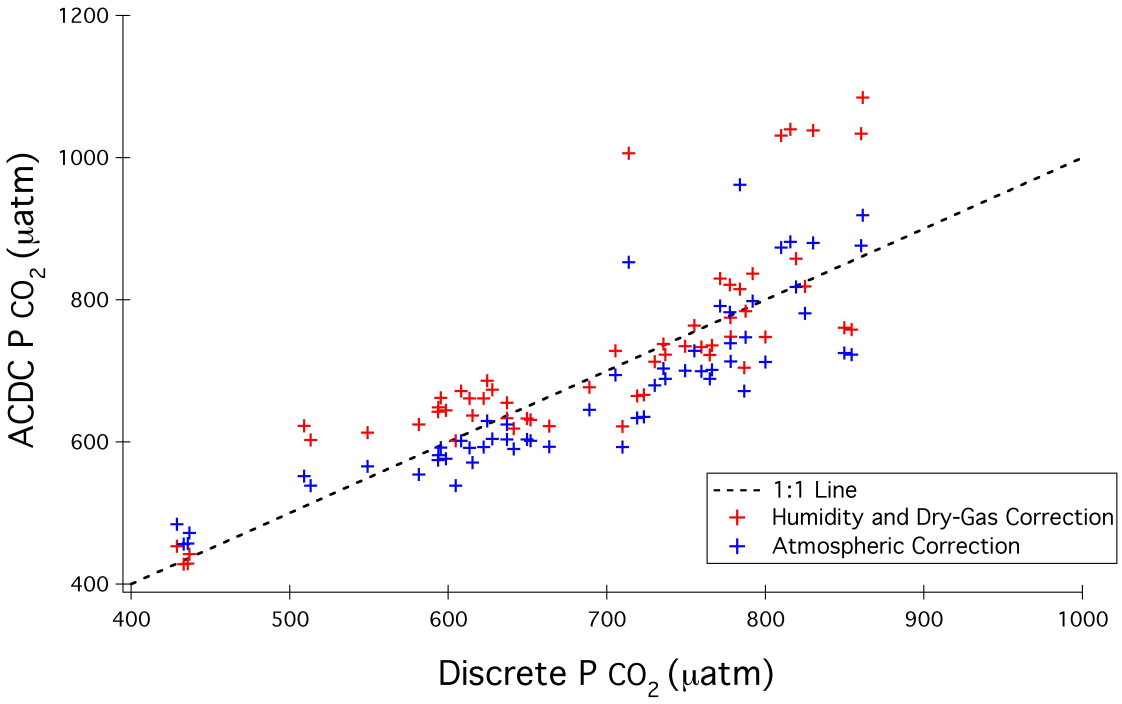

Figure 6: Validation Sample Comparison. This figure is a scatter plot of the ACDC instrument PCO_2 vs. discrete bottle sample PCO_2. The discrete sample time was time delayed by 17.9 minutes due to the modeled liquid response time. A value of *in situ* PCO_2 was then found that correlated with the time-delayed sample time of each discrete sample. The dashed black line is the 1:1 relationship line. The red crosses are values of PCO_2 that have been corrected for humidity and calibrated using the dry gas calibration curve. The blue crosses are the PCO_2 data that has been humidity corrected and dry-gas calibrated and also have a secondary correction factor applied. This correction factor was determined empirically from the atmospheric readings taken before each deployment.

$$\text{Average Relative Deviation} = \text{Average}\left[\frac{(\text{ACDC Value}) - (\text{Discrete value})}{(\text{Discrete Value})}\right]$$

Equation 13

Without performing this correction, the average relative deviation from check sample values is 4.1%, suggesting a positive bias in the ACDC results. Once the atmospheric correction factor is applied this deviation decreases to -2.5%.

I believe that the uncorrected ACDC data is positively biased from the discrete check sample data and that the application of the atmospheric correction factor overestimates the true ACDC value. The measure of the precision of the ACDC is given by calculating the average absolute deviation (Equation 14):

$$\text{Average Absolute Deviation} = \text{Average}\left[\frac{ABS[(\text{ACDC Value}) - (\text{Discrete value})]}{(\text{Discrete Value})}\right]$$

Equation 14

For the non-atmospherically corrected data, this measure of imprecision is 8.1%, once the atmospheric correction factor is applied, the scatter of the data decreases to 6.9%. I believe further efforts to better understand the drivers of the need for this correction should be taken in order to achieve more accurate ACDC P_{CO_2} data.

5.2 Response Time Effects on Field Performance

Throughout the various field and laboratory studies, I noted that the system's response time for P_{CO_2} signal equilibration was longer than expected. The bench-top system developed by Hales et al. (2004) has a P_{CO_2} response time of 3 seconds. This system has an experimentally determined response time of 17.9 minutes. Based on values of molecular diffusivity of carbon dioxide in air,

as well as the physical properties of our system, I believe our response time should be much faster. As discussed above, the slower-than-predicted responses to changes in ambient gaseous concentration suggest slower transport than gaseous diffusion, and the further slowed response to ambient aqueous changes suggests the barrier to diffusive transport caused by hydro-dynamics surrounding the equilibrator could be at fault. It is therefore important to recognize that stagnant environments will lead to an even slower response time and lower resolution data. Ideally, a response time would allow for proper resolution to visualize changes in the P_{CO_2} of the surface water column. At 17.9 minutes, there is most likely a great deal of smearing of any *in situ* P_{CO_2} signal that varies on shorter timescales.

6. Proof-of-Concept Data Sets

6.1 Eulerian Studies

Three Eulerian data sets were collected during the fall of 2013 on October 17, October 29, and November 1. Tidal predictions for these dates can be seen below in Table 2.

Date	HIGH				LOW			
	Time (PST)	Height (ft)	Time (PST)	Height (ft)	Time (PST)	Height (ft)	Time (PST)	Height (ft)
17-Oct	11:45	9.00	-	-	5:24	1.00	18:04	-0.20
29-Oct	9:28	6.87	21:29	6.00	2:44	1.57	15:41	2.37
1-Nov	11:08	8.29	-	-	4:54	1.91	17:46	0.09

Table 2: Tidal Predictions for Newport, OR

Figure 7 is a time series plot of both *in situ* (squares) and discrete (✖'s) P_{CO_2} data taken on the three non-consecutive sample dates with 17-Oct-13 is green, 29-Oct-13 is blue, and 01-Nov-13 is red. The discrete sample data was time delayed by 17.9 minutes in order to account for the response time delay. The *in situ* data was then averaged around each discrete sample time to create a time series of values. Data was plotted in tidal-time-space as minutes after the Mean Higher-High-Water (MHHW) tide of the day. This figure highlights the excellent correspondence of the discrete and *in situ* data.

6.2 Lagrangian Studies

Two Lagrangian Data sets were taken using the ACDC as a drifting P_{CO_2} system. The first on November 24, 2013 along the near-shore south of Newport, OR, and the second on December 18, 2013 in the Yaquina River between the Toledo Public Boat Launch (44°35.905' N, 123°56.36' W) and Cannon Quarry Park (44°32.230' N, 123°54.149' W). Drift maps of both deployments can be seen in Figure 8. These data sets involve the sensor drifting freely with the currents. While on the coastal ocean, I had the drifter secured with a 20 ft line to a small fishing vessel and maneuvered to maintain slack line and match the drift of ACDC. Winds that day were light and had minimal impact on the movement of the vessel or the drifter. The two 24-Nov-13 drifts are separated by color, with the first drift in pink and the second in green. An overlay of Pacific Coast NOAA Nautical chart #18580 was created to show depth soundings (in fathoms) in that region. The drift track for 18-Dec-13 is shown along the upper estuary near

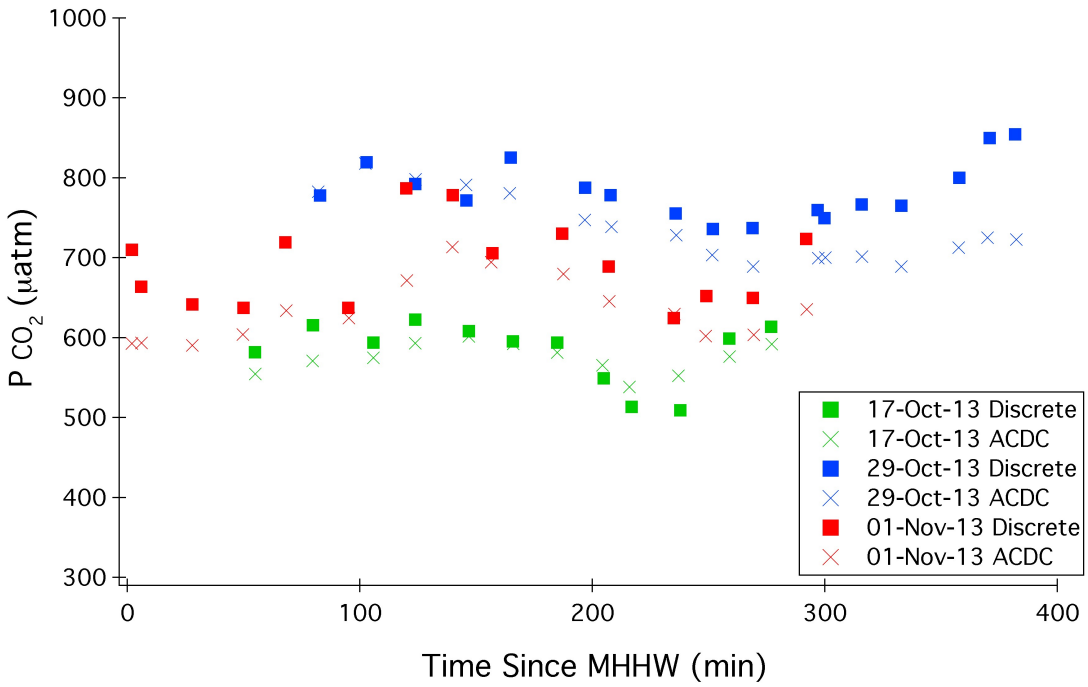

Figure 7: Eulerian time series data plots. A time series plot of *in situ* and discrete PCO_2 measurements. All data was taken in Yaquina Bay, Newport, OR on 17-Oct-13 (green), 29-Oct-13 (blue), 01-Nov-13 (red). Discrete measurements are shown as ✖'s and ACDC measurements are shown as squares. Time series data is plotted as minutes since Mean Higher-High-Water (MHHW).

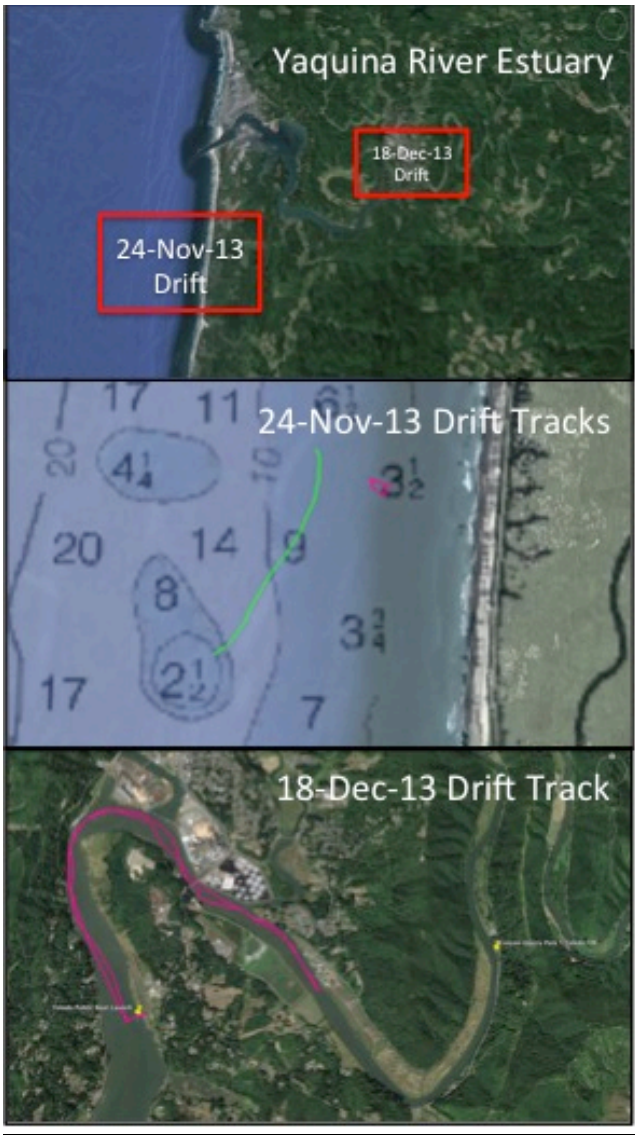

Figure 8: ACDC Drift Track Maps. The drift tracks are written in ".kml" code generated from the GPS positions logged by the sensor platform. For 24-Nov-13, Drift 1 is in pink and runs in a clockwise circle from the bottom right. Drift 2 is in green and runs northeast. Repositioning took place between Drift 1 and 2. Overlay of depth soundings (fathoms) has been created using NOAA nautical chart #18580, showing shallow pinnacles along the southern near-shore. For 18-Dec-13, markers have been placed to show the location of the Toledo Public Boat Dock and Cannon Quarry Park.

Toledo, OR with markers for the Toledo Public Boat Launch and Cannon Quarry Park. The ACDC moved up estuary with the flood current for approximately 4 hours before the tidal reversal forced it to drift back in the direction of the Toledo Public Boat Launch. Near dusk, the ACDC was recovered 1.5 miles up-river from the Toledo Public Boat Launch. Figure 9 shows time series plots of these two Lagrangian data sets as a function of time since deployment.

7. ACDC Data Set Discussion

Data collected by the ACDC system thus far only begins to capture the range of biogeochemical processes taking place in Oregon estuaries. I have shown that this new platform will be an ideal option to increase the understanding of the carbonate system through the (1) utility of *in situ* data collection versus discrete sampling followed by laboratory analysis, (2) continuous high resolution data collection, and (3) flexible autonomous and drifting capabilities. This new platform alleviates the need to compensate for *in situ* temperature, as the P_{CO_2} is measured continuously at *in situ* conditions. The ACDC sensor can be left to sample autonomously in foul weather and overnight and to produce useful P_{CO_2} data during times when human sampling is typically not in the field. Even an intensive discrete sampling program would be challenged to capture a fraction of the data this system is capable of producing, and at a significantly higher human-labor cost. As the ACDC is improved upon, the response time, and therefore resolution will be enhanced, surpassing any discrete sampling regimen.

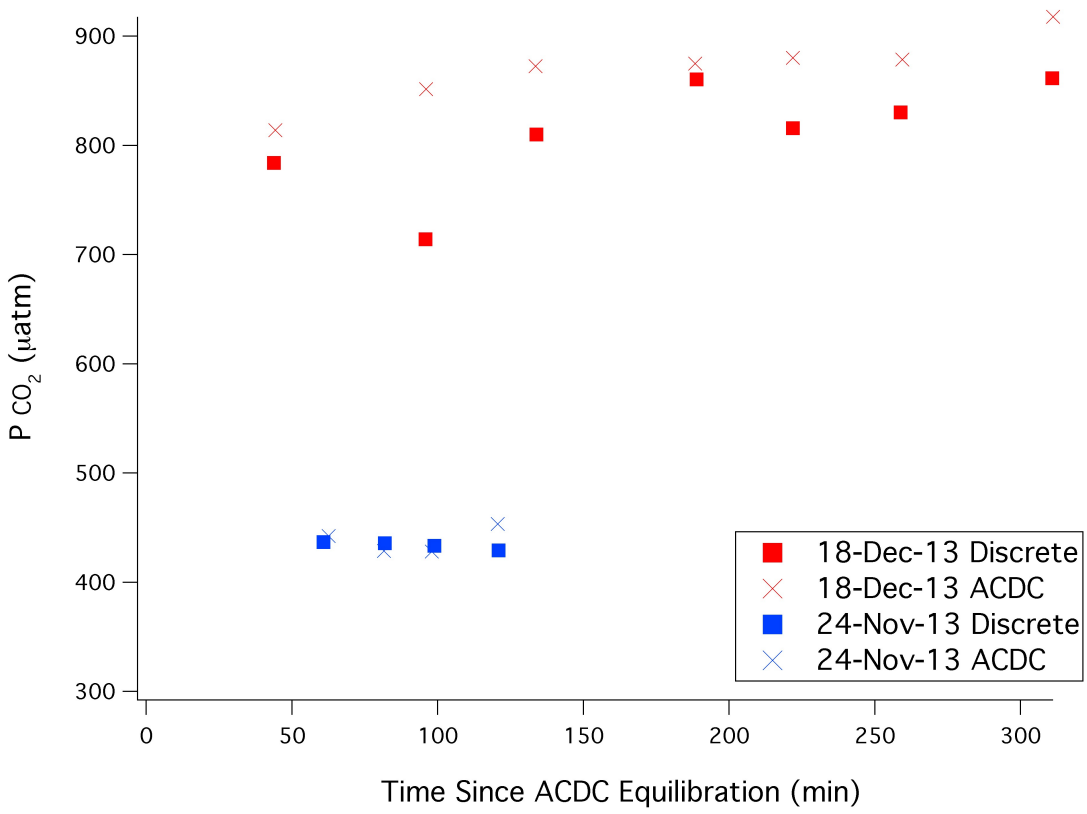

Figure 9: Lagrangian time series data plots. A time series plot of *in situ* (squares) and discrete (✖'s) PCO_2 measurements taken near Newport, OR on 24-Nov-13 (blue) and 18-Dec-13 (red). Time series data is shown as minutes since ACDC equilibration.

Despite the availability of continuous data collection possible with the ACDC, a coordinated discrete sampling program should be continued. To fully constrain the carbonate system of the estuary, a second parameter beyond P_{CO_2} is needed. The occasional measurement of a near conservative carbonate chemistry parameter such as DIC will allow for generation of predictive salinity dependences and thus the full calculation of all species in the carbonate system of the estuary. As deployment lengths increase, the discrete samples will also serve as a check for instrument functionality with regards to equilibrator and water probe bio-fouling, sensor drift, and low-battery complications.

The three Eulerian ACDC data sets were all taken in the lower YRE in very similar weather and tidal conditions. Similar ranges of P_{CO_2} can be see on all three days, with values ranging from approximately 500 – 800 μatm. The Lagrangian data sets show the difference between the river water and ocean water P_{CO_2}. The near-shore data collected on 24-Nov-13 has a near-atmospheric P_{CO_2} and was in close agreement with the discrete samples. The oligohaline region P_{CO_2} measurements, taken on 18-Dec-13 show the much higher P_{CO_2} expected in the upper estuary. From the high correlation of the in situ data to the discrete data, as shown in Figure 7, I believe that these time series of P_{CO_2} in the YRE accurately reflect the dynamics that occurred during the time of the ACDC deployments. By measuring the P_{CO_2} of the surface water instead of calculating P_{CO_2} from other parameter measurements as discussed above, the ACDC system portrays a more accurate view of the estuary and the data can then be used to calculate air-sea CO_2 fluxes for the YRE.

8. ACDC Conclusions

While this system is still in development, one clear advantage of the ACDC platform is its ability to take data autonomously over many hours while moored in a single location as opposed to sampling discretely, a procedure which is more user intensive. *In situ* data acquisition also does not involve preservation of the sample. In the upper estuary, where salinity is very low, the $HgCl_2$ preservative used will act as an acid, driving up the P_{CO_2} due to complexation with carbonate ions instead of chloride ions normally present in higher salinity waters. (Swanson and Hales, unpubl). The data collected by the ACDC system does not require temperature corrections from laboratory temperature back to in situ temperature as is necessary with discrete sampling methods, and frees estimations from assumptions regarding thermodynamic constants of the carbonate system.

It is obvious that the carbon community will benefit from data such as that collected by the ACDC system. Historic methods of estuarine observing leave more uncertainty than is acceptable when speaking in terms of the global carbon budget. The ACDC system is both stable and accurate as has been shown in both the bench-top and field-testing data. This system has shown to be both rugged and flexible making the ACDC suitable for a myriad of deployment strategies in various environments including estuaries and the near-shore.

III. Seasonal Estuarine Sampling Program

During the 2013 calendar year, over 200 discrete samples were collected from the YRE, Alsea River Estuary (ARE), and Netarts Bay (NB), all macro-tidal estuaries located on the Pacific Coast of North America. While geographically proximal, these estuaries represent a range of conditions. The YRE that was the focus of this work is a high-volume, moderately low-freshwater input estuary with relatively long water residence times with respect to both river and tidal exchange. Netarts Bay is a shallow, small-volume bay with almost no freshwater input, but is nearly flushed with each tide. The Alsea River estuary is intermediate in volume, with a significantly larger riverine input than the YRE. Figure 10 shows four plots of the properties (clockwise from top left) DIC, T_{Alk}, water temperature, and PCO_2 all in Salinity space. All data collected for the seasonal estuarine sampling program is displayed in this figure. Two distinct groups emerge in the data: 1) The data colored brown shows a strong correlation of the property to salinity for both DIC and T_{Alk} and 2) the dark blue colored data that clusters at the high salinity values and shows weaker trends with respect to salinity over the sampling time. The first group of data shows estuarine properties consistent with effects from a local freshwater source during high seasonal river discharge rates. The second group of data shows influences from the ocean during very low discharge time periods for the local rivers.

In Figure 10, data collected from NB is colored green, and not included in either of these two groups, as the data does not follow either of the aforementioned trends. NB has almost no local freshwater source of its own and therefore has non-typical estuarine processes within its boundaries. The data for

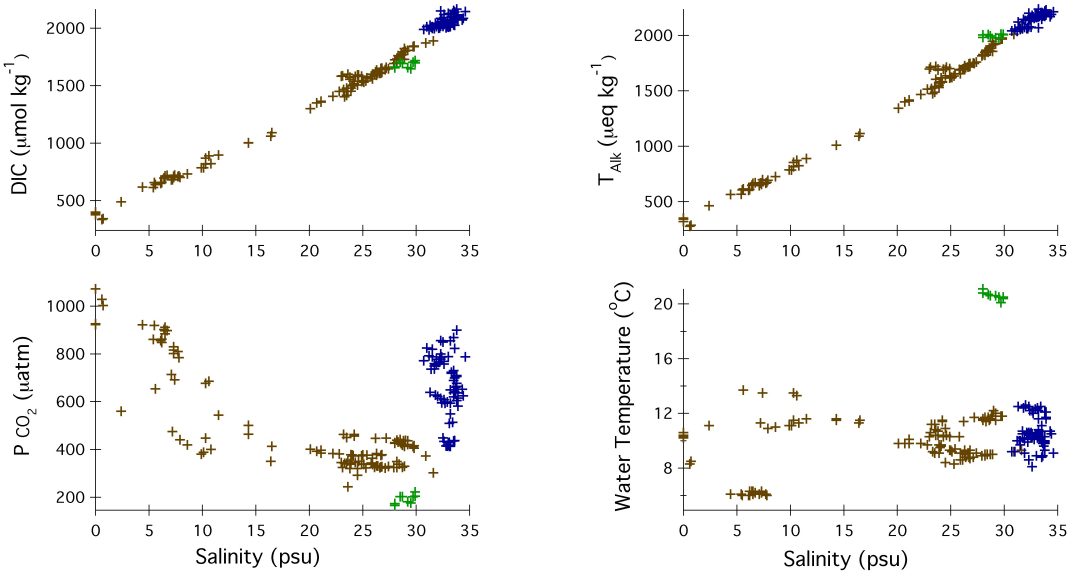

Figure 10: All estuary data points obtained in study. Clockwise from top left is DIC, T_{Alk}, PCO_2 and Water Temperature plotted in salinity space. Brown crosses indicate local freshwater source dominated estuary samples. Blue crosses indicate non-local freshwater source dominated estuary samples. Green crosses were obtained in Netarts Bay, OR.

NB was collected on 03-Jul-13 when eelgrass growth on the shallow estuarine sediments is maximal; water temperatures were high due to strong insolation of the shallow water column. The NB data has been omitted for the rest of the discussion.

1. Local Freshwater Controls

Using the DIC, T_{Alk}, and water temperature values obtained by collecting both ocean and freshwater endmembers, I calculated conservative mixing curves for the YRE and ARE. Mixing curves display a predicted relationship based on conservative mixing of the two endmembers, that is, to mix without the consumption or production of any property in the estuary. The conservative mixing line for P_{CO_2} was calculated from the predicted values of DIC, T_{Alk}, and a water temperature of 10^{o}C using “carbcalc”, a program developed by B.Hales at Oregon State University. Discrete values for all properties were then plotted against their measured salinities. Figure 11 displays conservative mixing curves and discrete data where the property to salinity relationship is driven by the mixing of a local freshwater source (either the Yaquina or Alsea River) and the Pacific Ocean. The P_{CO_2} values for the discrete samples have been temperature corrected to 10^{o}C by “carbcalc”. This data was collected predominantly in the winter and early spring (9-Jan-13, 7-Feb-13, 7-Mar-13, 14-Apr-13, 19-Apr-13) in the lower estuary, a time period marked by higher freshwater flows from the estuary’s associated river; however, the data set taken in the upper YRE on 18-Dec-13 is also included.

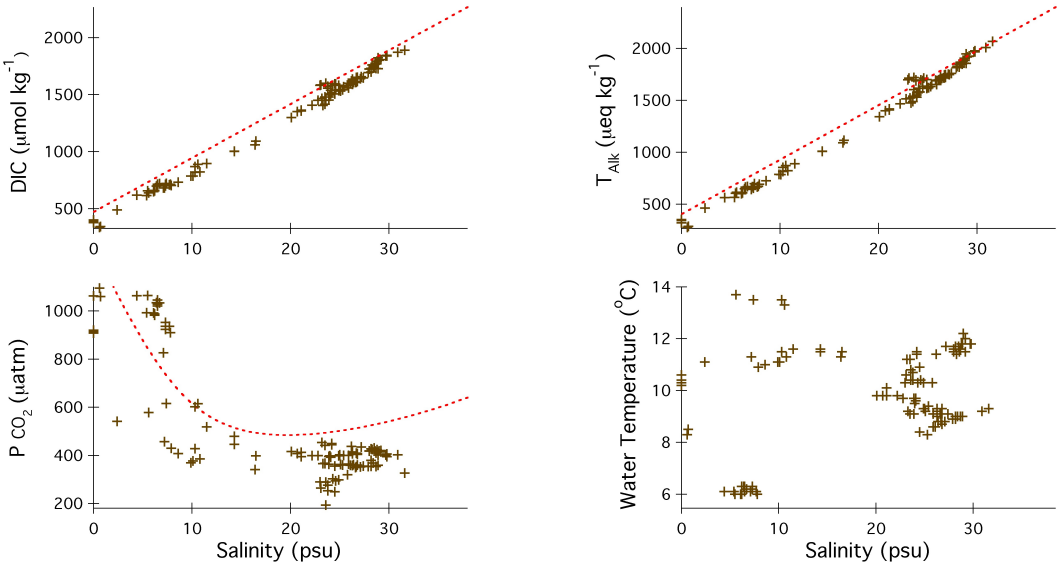

Figure 11: Local-freshwater source dominated estuary data. Clockwise from top left is DIC, T_{Alk}, PCO_2 and Water Temperature plotted in salinity space. Brown crosses are the discrete sample data points for each property. The red-dashed lines indicate representative conservative mixing curves for predicted values of DIC, T_{Alk}, and PCO_2.

From the predicted mixing curves, a plot of the residuals for T_{Alk} vs. DIC is shown in Figure 12. Residuals, calculated as the conservative mixing predictions minus the observations, show up as positive values for properties that are consumed within the estuary, and negative for properties that are produced. This figure is color-coded by sample salinity to represent the gradient over which the discrete samples were collected. Residuals from the predicted conservative mixing line can offer suggestions as to the biogeochemical processes that drive these deviations. Results, presented in Figure 12, show that there are significant additions and subtractions of both T_{Alk} and DIC from the conservative mixing prediction, and that the residuals of these properties are strongly positively covariant. The possible reasons for these distributions are discussed below.

2. Local Coastal-water controls

Similar property-salinity plots were created in Figure 13 for the data mostly collected in the lower estuary during Fall (17-Oct-13, 29-Oct-13, 1-Nov-13, 24-Nov-13), times of very low river discharge into the estuary preceding the typical seasonal increase in precipitation and river discharge. Although the salinity range is relatively small, it is evident that these data deviate from the mixing line and the observations from the higher local-discharge conditions shown for reference in Figure 12. The tendency for these data to deviate from the local-source mixing line towards higher T_{Alk} and DIC will be discussed below.

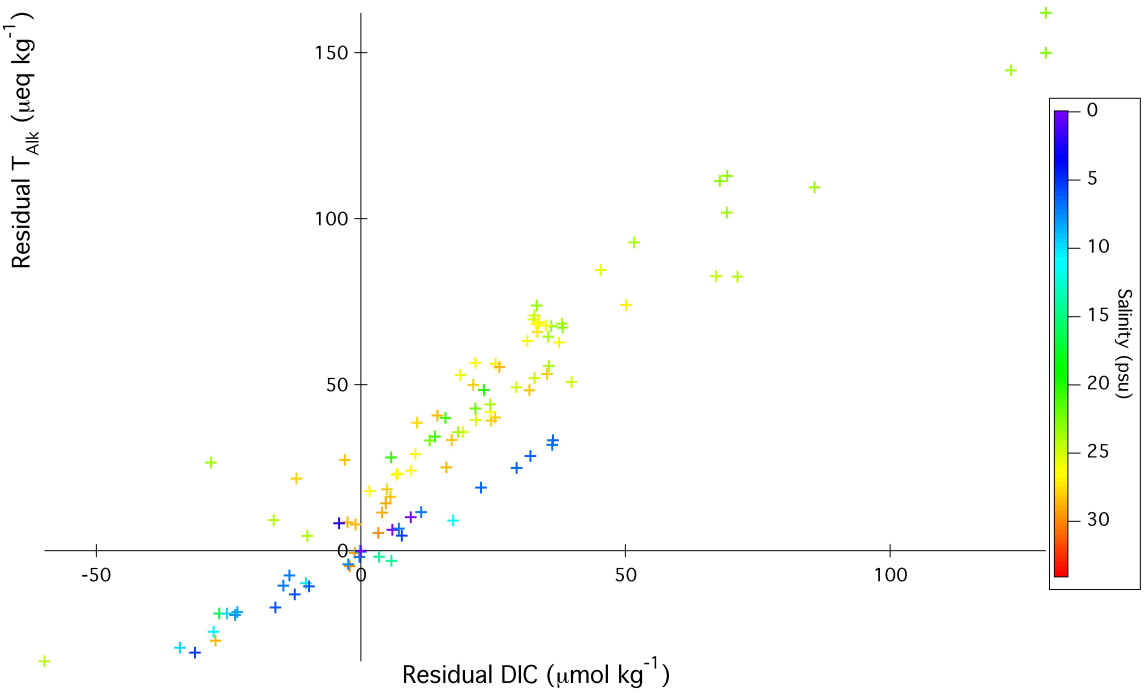

Figure 12: Residuals of the actual T_{Alk} (y-axis) and DIC (x-axis) from the conservatively predicted values. Data points are color coded by salinity with respect to the color bar on the right. Positive residuals represent within-estuary consumption; negative residuals represent within-estuary release.

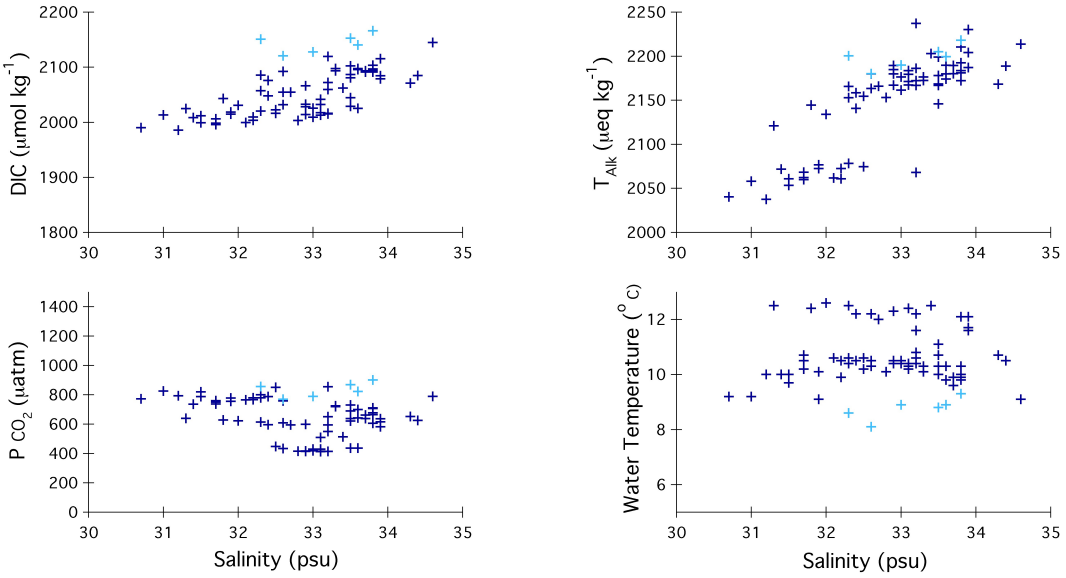

Figure 13: Non-local-freshwater source dominated estuary data. Clockwise from top left is DIC, T_{Alk}, PCO_2 and Water Temperature plotted in salinity space. Dark blue crosses are the discrete sample data points for each property. Light blue crosses indicate data acquired during a mild-upwelling event in the Alsea Bay.

3. Air- Sea CO_2 Flux Estimations

From the discrete PCO_2 data gathered during this research in the YRE only, I have calculated an areally-integrated air-sea CO_2 flux. The flux (F, mmol m^{-2} d^{-1}) is calculated according to Equation 1. The $PCO_{2\,(air)}$ was measured by the instrument package while on the pier prior to commencing data collection and corrected as discussed above. Various dependences have been suggested for dependence of the aqueous gas transfer velocity of CO_2 on wind and current speeds. These equations often are used for calculations in the open ocean where gas transfer is predominantly caused by wind stress on the water surface. However, in an estuary, it is a combination of factors as discussed previously such as tidal forcings and estuary bed friction. To calculate k_w of this estuary, I used Equation 15 below from Jiang et al. (2008):

$$k_w = (0.314U_{10}^2 - 0.436U_{10} + 3.99) \times \left(\frac{Sc_{SST}}{660}\right)^{-0.5}$$

Equation 15

where U_{10} (m s^{-1}) is the average wind speed over the deployment period as measured at the Newport Regional Airport (44°34.817' N, 124°3.483' W) 5.13 km from the mooring site. Sc_{SST} is the Schmidt number scaled to Sea Surface Temperature (SST, °C) as measured for each discrete sample. Once I had calculated air-sea CO_2 fluxes for each data point, I plotted the air-sea CO_2 flux against salinity (Figure 14). This figure shows that the data can be grouped into three regions based on their salinities.

For reference purposes the three regions will be referred to as the oligohaline, polyhaline, and mixoeuhaline regions. I made estimations of the area

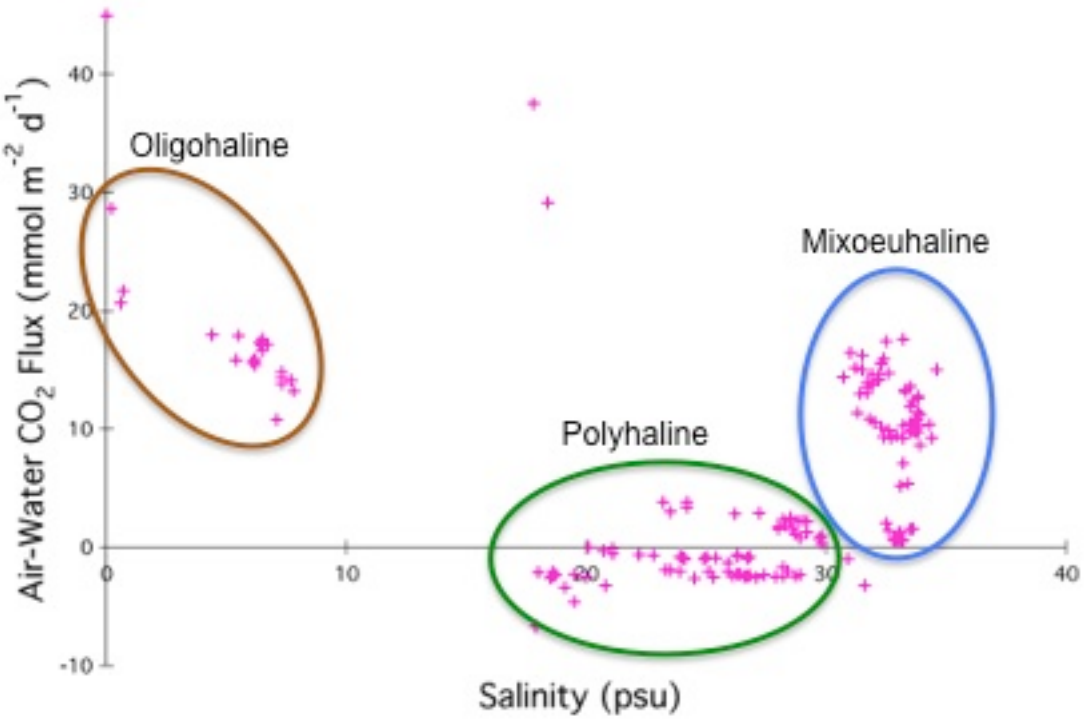

Figure 14: Discrete Sample Air-Water CO_2 Flux. Fluxes were calculated for each discrete value of $PCO_{2\,(water)}$ and then plotted in salinity space. The resulting three regions are, from left to right, oligohaline, polyhaline, and mixoeuhaline.

covered by each of these salinity regions based the salinity patterns observed in both my discrete bottle data and that from two cruises in the YRE in 2012 and 2013 (Prahl, unpubl). I chose the mixoeuhaline region to cover from the mouth of the jetties to the southeastern 90^{o} river bend, the polyhaline region to cover from that 90^{o} bend to the Toledo Public Boat Launch, and the oligohaline region to cover from the Toledo Public Boat Launch up to Cannon Quarry Park. Canon Quarry Park is below the actual head-of-tide for the Yaquina River, however, as the river narrows beyond this point, the significance of the air-sea CO_2 fluxes becomes minimal due to decreasing area of the river. These regions can be seen in Figure 15, annotated on a map of the YRE from Google Earth. I estimated polygonal water-surface areas for each of these regions and then multiplied those areas by the average flux of each region, and then summed those products to calculate an areally-integrated air-sea CO_2 flux of 4.5 x 10^7 mol CO_2 y^{-1} off-gassed by the YRE. To calculate an area-weighted average air-sea CO_2 flux, I divided the areally-integrated air-sea CO_2 flux by the total area of the estuary estimated from Figure 15 (16 km^2) and found a value of 3 mol C m^{-2} y^{-1} off-gassed from the YRE. Table 3 summarizes the estimated areas and average air-sea CO_2 fluxes calculated from the discrete data.

Region	Area	Average Flux	Region Flux
	m^2	mol C m^{-2} y^{-1}	mol C y^{-1}
Mixoeuhaline	1.0E+07	3.5	3.5E+07
Polyhaline	4.6E+06	0.066	3.0E+05
Oligohaline	1.4E+06	6.6	9.3E+06

Table 3: Areally Integrated Air-Sea CO_2 Flux

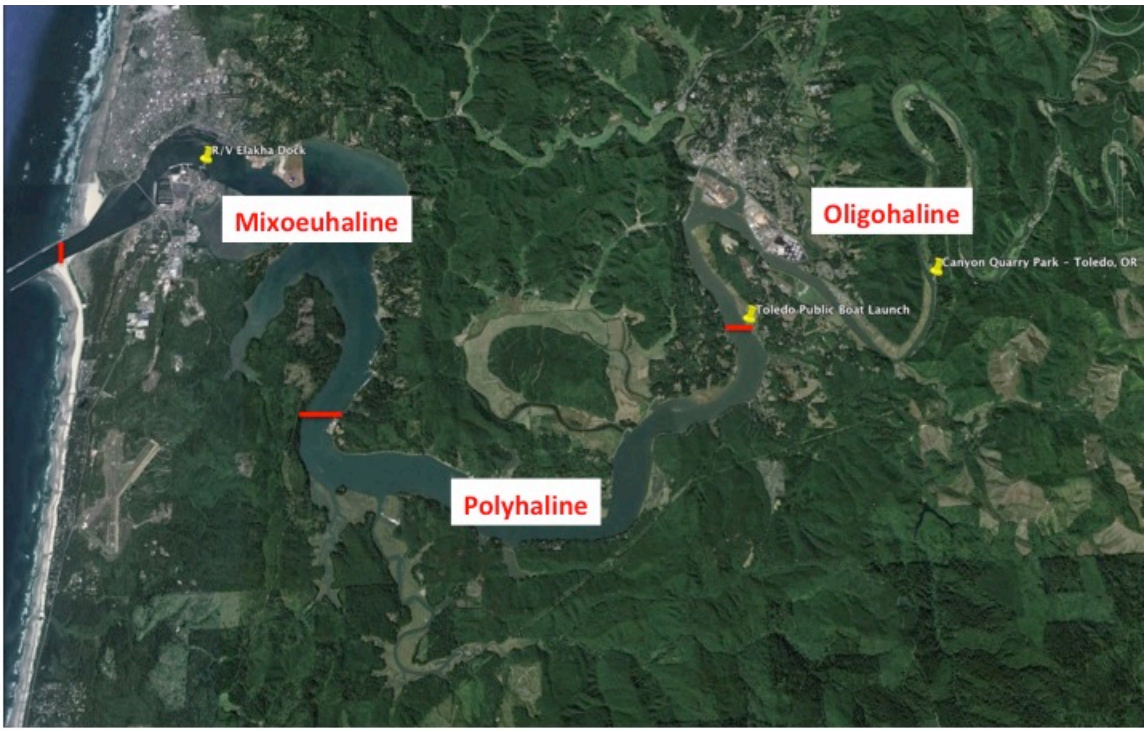

Figure 15: Flux-salinity region area estimations. The area of each region from Figure 14 was calculated based on estimated area of the salinity range. The solid red lines indicate the extent of each region for areal estimation purposes. Markers for the R/V Elakha Dock, Toledo Public Boat Launch, and Cannon Quarry Park are shown for reference only.

While I believe these regions accurately reflect the salinity gradients observed throughout this study, it should be mentioned that the YRE has seasonality to the range of salinity at various points. The regions I determined were based on seasonally and temporally biased check samples (as discussed previously). However, for the purpose of this study, and the estimations made for the air-sea CO2 flux for the YRE, I believe these regions to reflect the average trends in the YRE salinity gradient.

4. Discussion

The sampling program carried out in 2013 in Yaquina and Alsea Bays provided a large quantity of discrete samples to be analyzed for DIC and P_{CO_2} resulting in a great deal of information about these coastal macro-tidal systems. It is known that these SMRS have a high variability in their freshwater discharge as a result of seasonal rain and drought cycles. The data collected in this study supports this by showing the different dominating forces in the YRE and ARE throughout the year.

4.1 Local-Freshwater Source Dominated Estuarine Processes

In the winter and early spring, rainfall in the Coastal Oregon range can exceed two meters (Hatten et al. 2010). This results in a large increase in the freshwater discharge from rivers into their associated estuaries. Figure 11 shows evidence of the higher freshwater discharge time period of the YRE and ARE by the near-conservative relationship between DIC and T_{Alk} with salinity. Figure 11

shows a red dashed line to indicate the conservative mixing line drawn between the freshwater and ocean endmembers for DIC and T_{Alk}. The data falls nearly on the line over a large salinity range as the freshwater and oceanwater mix in the estuary.

The water temperature versus salinity plot, shown on bottom right of Figure 11, shows very little conservation with mixing between the freshwater and saltwater endmembers, even though daily temperature to salinity relationships were strong. In response to the apparent non-conservative nature of water temperature, I temperature corrected the P_{CO_2} values to 10^{o}C to remove any artifact from this effect. The P_{CO_2} values shown on the bottom left plot do show a similar downward curved trend towards low P_{CO_2} values at high salinity. The discretely measured values of P_{CO_2} do not, however, fall as conservatively on the predicted mixing line as do the DIC or T_{Alk} values. This is a result of the fact that PCO_2 is highly non-linearly dependent on variations in the T_{Alk}: DIC ratio.

Figure 12 shows the ΔT_{Alk} : ΔDIC based on the residuals between observed and predicted conservative-mixing values for the discrete data during months of local freshwater source influence on the estuaries. The slopes of each data set shown in Table 3 below describe the ~1:1 or greater ratio seen in the residual data.

Date	$\Delta T_{Alk}/\Delta$DIC
9-Jan	1.4
7-Feb	1.2
7-Mar	1.3
14-Apr	1.0
19-Apr	0.8
18-Dec	0.9

Table 4: ΔTAlk : ΔDIC ratios

There are many biogeochemical processes affecting this ratio in different ways, however, only $CaCO_3$ dissolution and precipitation (Equation 16) can lead to both positive and negative residuals with ΔT_{Alk}: ΔDIC above 1.

$$\mathrm{CaCO_3} \leftrightarrow Ca^{2+} + CO_3^{2-}$$

Equation 16: Calcium Carbonate Reaction

Net photosynthetic production and aerobic respiration proceed with a ΔT_{Alk}: ΔDIC of -0.15:1, much lower than, and of opposite sign to, the observed ratios. Gas exchange can lead to positive and negative DIC residuals, but has no effect on T_{Alk}. The progression of subaerobic metabolic processes that likely occur in the sediments and tide flats of the bay can lead to various ΔT_{Alk}: ΔDIC ratios, but only sulfate reduction (Equation 17) has a large production of T_{Alk} relative to DIC:

$$2CH_2O + SO_4^- \rightarrow H_2S + 2HCO_3^-$$

Equation 17: Sulfate Reduction Reaction

Sulfate reduction contributes to T_{Alk} and DIC equally, giving a ΔT_{Alk}: ΔDIC of 1:1; however, there is no corresponding reverse reaction, and sulfate reduction can only lead to negative residuals, given our definition above.

The observed ΔT_{Alk}: ΔDIC ratios are almost certainly the result of many estuarine processes, and we unfortunately do not have the ancillary data that would be required to quantify the relative contributions of each, nor can we determine the rates of these processes. However, there is no way to describe the positive and negative residuals of T_{Alk} and DIC with ratios consistently ≥1 without invoking $CaCO_3$ precipitation and dissolution. This finding shows the importance of this process even in estuaries that are not renowned as being

areas of extensive shell deposits, as, for example, is the Chesapeake Bay (Waldbusser et al. 2011)

4.2 Non-local Freshwater Source Dominated Estuarine Processes

The data collected during low local-river discharge periods shows different characteristics than the rest. First, this data shows a small salinity range over the entire tidal period of only ~3 psu, as seen in Figure 14. The DIC, T_{Alk}, and P_{CO_2} data cluster together at high values of salinity instead of showing any variability in salinity over the tidal efflux from the estuary. There are a few possible causes for this behavior. Groundwater input may be a factor, which in many locations is characterized by high T_{Alk} in fresh waters. Local stream hydrological experts report that river freshwater is dominated by groundwater in low-precipitation periods (J. McDonnell, OSU, pers. comm. to B. Hales, 2006); however, my direct observations of the freshwater sources show little deviation in this period from the low-T_{Alk} values seen in other times of the year. If groundwater chemistry were the cause of the difference in the chemical properties seen in the samples, it would have to shift not only the properties of the discrete samples of the turning basin, but that of the river endmember. Since the river endmember samples remain relatively constant over the entire year, this variation in chemical composition cannot be attributed to groundwater alone. While a serendipitous coincidence of groundwater and shell dissolution inputs that combine to yield property-salinity dependences matching the local open coastal waters can't be discounted, it is not the most simple and robust explanation.

The lower discharge rates of the river increases the residence time for freshwater in the estuary during these months lending to potential for a greater degree of biogeochemical modification of the property-salinity relationship. However, the residuals of the low-discharge observations all suggest a tremendously large generation of both T_{Alk} and DIC in only the most saline reaches of the estuary during relatively quiescent conditions when nutrient levels are still high enough to support net primary productivity. A longer time for biogeochemical processes to act on carbon in the estuary would also not explain the signals seen in the data. If the local estuary-based biogeochemical processes were driving the variability of the DIC and T_{Alk}, I would expect to see this variability over an observed salinity gradient. This is not the case, as seen in Figure 13 where the data clusters at high salinities.

The last explanation for the difference in estimated zero-salinity DIC and T_{Alk} over the year, and the most likely, is a remote influence on the estuaries during the low local freshwater discharge time period. The property-salinity relationships seen here are dominated by the variability of the coastal ocean, as opposed to the dilution of ocean waters with local riverine freshwater sources. Regression of these data versus salinity, despite the relatively low salinity range, is highly significant ($R^2 \cong 0.68$), and results in a T_{Alk}: S slope of 48.9. This slope is similar to that reported by Cullison-Gray (2011),as found to most appropriately merge with the in situ P_{CO_2} and pH data collected at the NH10 mooring directly seaward of YRE (Harris et al. 2013). While the salinity range is small, the implied freshwater end-member $T_{Alk} \cong 1000$ μeq kg^{-1} is about triple that for our

observations of local freshwater river sources throughout the season, and more consistent with the largest regional freshwater rivers, the Sacramento (T_{Alk} = 960 μeq kg^{-1}; Sacramento River Water NAWQA Program) and the Columbia (T_{Alk} = 1100 μeq kg^{-1}; Evans et al. 2013). Historical interpretations of the freshwater sources of the open Oregon coast have shown previously that salinity values below 32 are driven largely by the Columbia River plume (Huyer 1977).

The discrete sample set collected on 25-Apr-13 in the ARE (Figure 13, light blue) shows properties consistent with an upwelling event. The colder water, high DIC: T_{Alk}, and higher P_{CO_2} that occurred on this sampling date are all effects of upwelling in the estuary. Late April is early for an estuary to experience an upwelling event, however it was noted on this day that winds were coming out of the North causing this dynamic to occur. The high P_{CO_2} levels in upwelled water have been a topic of much study recently due to their effects on the commercial oyster fishery of the Pacific Northwest. Higher levels of P_{CO_2} result in a lower saturation state (Ω) for calcite and aragonite, both forms of $CaCO_3$. The lower Ω values adversely affect the larval bivalves ability to precipitate necessary biogenic minerals in their early life stages (Waldbusser et al. 2013)

4.3 Air-sea CO_2 Flux Estimations

The area-weighted average air-sea CO_2 flux calculated for the YRE from this research is a source, as implied by the global compilations, but appears to be much lower than those studies imply. The efflux can be compared to other values of estuarine CO_2 flux when similar methods of P_{CO_2} determination were

used. The Columbia River Estuary (CRE), located approximately 180 miles north of the YRE along the Oregon Coast is the terminus of the largest river in North America associated with a coastal upwelling system (Roegner et al. 2011). Evans et al. (2013) utilized the underway P_{CO_2} measurement system of Hales et al. (2004) for five cruises in the CRE over a two year period. From these cruises, they calculated the net annual air-sea CO_2 flux of 1 mol C m^{-2} y^{-1} using Equations 1 and 13. A micro-tidal estuarine study by Crosswell et al. (2012) performed in the Neuse River Estuary (NRE) in North Carolina, USA, consists of seven surveys from the upper to the lower estuary over a one year period. A setup similar to that of Hales et al. (2004) was used for continuous P_{CO_2} quantification. Once again, utilizing Equations 1 and 15 for calculating air-sea CO_2 flux, Crosswell et al. (2012) found an efflux of 5 mol C m^{-2} y^{-1}. Both of these values fall within the same order of magnitude as that calculated by the discrete sampling program I carried out. The reasonable consistency between my calculated flux values and those discussed here, regardless of the size or water quality of the study area, leads to the strong assumption that when fluxes are based on measured P_{CO_2} values, instead of calculated P_{CO_2} values, the resulting air-sea CO_2 flux is smaller and more accurately reflects the dynamics of the estuary.

When the YRE area-weighted average air-sea CO_2 flux is compared to other studies where the P_{CO_2} values used to determine the flux were calculated instead being measured, it is quickly seen how the uncertainty in estuarine DIC, T_{Alk}, and pH effects the P_{CO_2} calculations. The air-sea CO_2 flux for the Satilla River Estuary located in Georgia, USA, was calculated and described in Cai and

Wang (1998) to be 43 mol C m^{-2} y^{-1}. Frankignoulle et al. (1998) gives an overview of many European estuaries. The P_{CO_2} of these estuaries was calculated from measurements of DIC, T_{Alk}, and pH and then the air-sea CO_2 flux was estimated. The average efflux from these estuaries was 57 mol C m^{-2} y^{-1}. A study by Abril et al. (2003) focused on the Loire Estuary in Northern France, and using calculated values of P_{CO_2}, the air-sea CO_2 flux was found to be 64 mol C m^{-2} y^{-1}. These estuaries all found air-sea CO_2 flux values an order of magnitude greater than that found in the YRE. I believe one main reason for this is the method used to determine the P_{CO_2} of the water, that is, measuring P_{CO_2} vs. calculating P_{CO_2}. An additional potential reason for higher P_{CO_2} values in these estuaries compared to those of the Pacific Northwest of North America is the degree of human impact on the ecosystems. The estuaries studied by Frankignoulle et al. (1998) are all located in Northern Europe and have seen the effects of a large nearby human population over millennia. The result is a higher air-sea efflux of CO_2 from the estuary driven by anthropogenic input of excess carbon into the rivers that feed these estuaries.

I used Equation 15 to calculate the gas transfer velocity for CO_2 in my air-sea CO_2 flux estimations. This equation better estimates k_w at higher wind speeds than equations of Raymond and Cole (2001), as the regressed data used by Jiang et al. (2008) includes a larger range of wind speeds. However, if very low wind speeds were used to calculate k_w, it would appear that gas exchange finds a minimum and begins to increase. Wanninkhof (1992) gives another equation for estimating k_w that is a straight quadratic:

$$k_w = 0.31 \times U_{10}^2 \times \left(\frac{Sc}{660}\right)^{-0.5}$$

Equation 18: Wanninkhof (1992) k_w Equation

When applied to Equation 1, Equation 18 predicts that at a wind speed of zero, there is no gas exchange. It is important to illustrate the difficulty in properly determining the gas transfer velocity of the study environment when attempting to estimate air-sea CO_2 exchange, as both the chosen method and variability of environmental factors influence the accuracy of the final estimate.

5. Conclusions for the Discrete Sample Program

This portion of my research focused on discrete samples analyzed for PCO_2 and DIC in Yaquina and Alsea Bays taken over the course of a year in conjunction with a separate instrument development program. The data I collected showed that both estuaries were subject to different influences over the course of the data collection. The data showed that the level of freshwater discharge from the local river had significant effects on the chemical and physical properties of the estuaries. The presence of a great deal of precipitation in the winter and early spring caused the chemical properties of the estuary to become closely dominated by mixing between the ocean and freshwater endmembers. In the summer and early fall, the seasonal drought occurring each year in these watersheds lessens the influences of the local rivers. Therefore the ocean dynamics and properties, combined with a freshwater source moving down the Pacific Coast from the Columbia River Estuary, act to dominate the property-salinity relationships.

An area-weighted average air-sea CO_2 flux was calculated for the YRE from the discrete sample P_{CO_2} values. This CO_2 efflux, estimated at approximately 3 mol C m^{-2} y^{-1}, is similar to other studies with comparable approaches to P_{CO_2} determination of the estuary. In studies where P_{CO_2} was calculated from measured values of pH, DIC, or T_{Alk}, the resulting air-sea CO_2 flux was an order of magnitude greater than that estimated in the YRE for this study due to the complex chemistry in these ecosystems and the sensitivity of the calculated P_{CO_2} to these drivers.

IV. Conclusions and Future Work

In this research I have presented a novel method for continuous P_{CO_2} quantification, *in situ,* as either a drifting or moored sensor with flexible deployment capabilities and mooring schemes. The data collected by ACDC and presented here correlates extremely well with both internally collected discrete samples as well as with other studies in similar environments using comparable gas equilibration techniques. Estuaries require exhaustive year-round measurements for multiple seasonal cycles in order to acquire enough data to compose an accurate representation for these unique systems. Our system, with its low power requirements, minimal required user-interaction, and highly flexible deployment strategies will allow for these comprehensive measurements to be made in the coming years.

While this system has surpassed our expectations in accuracy and low-cost initiatives, there are many improvements I hope users will make in the

future. The first improvement needs to be decreasing the response time, which currently is limited by both gas exchange surface area and water mixing rates in the vicinity of the equilibrator. I believe that an upgraded equilibrator design and meticulous bench testing to refine the ideal plumbing scheme will decrease the response time of the system thereby increasing the resolution of the continuous P_{CO_2} data stream. I currently make pressure and humidity corrections to both our system and the discrete sample bottles. Ideally, the *in situ* platform will not require these compensations in the future. The same company that supplies the K-30 CO_2 sensors used in this research also has built a next generation CO_2 sensor with integrated humidity and temperature sensors (www.co2meter.com, #SE-0027) within the NDIR chamber. These measurements would be invaluable for proper compensation in the future yielding the most precise P_{CO_2} measurements to date.

With the flexibility of the Arduino micro-controllers, there is a possibility for integrating different serial and analog sensors into this system. The same company which supplies the K-30 CO_2 sensor also makes an oxygen sensor (www.co2meter.com, #CM-0201) which has a 0 – 25% O_2 measurement range, pressure and temperature compensation, and UART communication protocols. This sensor could easily be integrated into the gas plumbing loop and provide measures of oxygen in the water. Recent work with industrially produced ion sensitive field effective transistors (ISFETs) for measuring seawater pH by Martz et al. (2010) shows proof of concept with these fast and stable sensors in surface ocean waters out to 600 km from shore. A combination of pH and P_{CO_2}

measurements can be used to constrain the entire aqueous carbonate system. This stable and reliable method for measuring pH would be a desirable addition to the ACDC system described here.

The utility of this sensor also has ecological implications. The ability of this sensor to drift with the tidal currents of an estuary, similar to the motion of a larval bivalve, may help scientists to better understand the perils faced by these organisms in a new regime of higher P_{CO_2} and lower saturation states for $CaCO_3$. Work being done at Whiskey Creek Shellfish Hatchery in Netarts Bay, OR has already shown the effects of ocean acidification on the commercial oyster fishery (Barton et al. 2012). Future work with the ACDC system to employ a network of sensors in the bay continuously monitoring P_{CO_2} throughout seasonal upwelling events, tidal excursions, and diel cycles will be promising in supporting and adapting this multi-million dollar industry.

As the ACDC system is further developed and its sensor suite customized for the variety of applications available, the scientific community will benefit from precise *in situ* quantification of the near-shore and estuarine carbonate cycle as well as an improved understanding of the role of these ecosystems in the global carbon system and the role we, as humans are playing in changing the biogeochemical properties of our most important natural resource.

Bibliography

1. Abril, Gwenaël et al. “Carbonate Dissolution in the Turbid and Eutrophic Loire Estuary.” *Marine Ecology Progress Series* 259 (2003): 129–138. Print.
2. Alin, Simone R. et al. “Physical Controls on Carbon Dioxide Transfer Velocity and Flux in Low-Gradient River Systems and Implications for Regional Carbon Budgets.” *Journal of Geophysical Research* 116.G1 (2011): n. pag.
3. Ambrose, D., and I. J. Lawrenson. “The Vapour Pressure of Water.” *The Journal of Chemical Thermodynamics* 4.5 (1972): 755–761. Print.
4. Borges, AlbertoV. “Do We Have Enough Pieces of the Jigsaw to Integrate CO2 Fluxes in the Coastal Ocean?” *Estuaries* 28.1 (2005): 3–27.
5. Broecker, Wallace S., and Tsung-Hung Peng. *Tracers in the Sea*. Lamont-Doherty Geological Observatory, Columbia University, 1982. Print.
6. Broecker, Wallace S., and Taro Takahashi. “Calcium Carbonate Precipitation on the Bahama Banks.” *Journal of Geophysical Research* 71.6 (1966): 1575–1602.
7. Cai, Wei-Jun. “Estuarine and Coastal Ocean Carbon Paradox: CO2 Sinks or Sites of Terrestrial Carbon Incineration?” *Annual Review of Marine Science* 3.1 (2011): 123–145.
8. Cai, Wei-Jun, and Yongchen Wang. “The Chemistry, Fluxes, and Sources of Carbon Dioxide in the Estuarine Waters of the Satilla and Altamaha Rivers, Georgia.” *Limnology and Oceanography* 43.4 (1998): 657–668. Print.
9. Cai, Wei-Jun, Yongchen Wang, and Robert E. Hodson. “Acid-Base Properties of Dissolved Organic Matter in the Estuarine Waters of Georgia, USA.” *Geochimica et Cosmochimica Acta* 62.3 (1998): 473–483.
10. Callender, Edward, and Douglas E. Hammond. “Nutrient Exchange across the Sediment-Water Interface in the Potomac River Estuary.” *Estuarine, Coastal and Shelf Science* 15.4 (1982): 395–413.
11. Carr, Mary-Elena. “A Numerical Study of the Effect of Periodic Nutrient Supply on Pathways of Carbon in a Coastal Upwelling Regime.” *Journal of Plankton Research* 20.3 (1998): 491–516.
12. Chen, Chen-Tung Arthur, and Alberto V. Borges. “Reconciling Opposing Views on Carbon Cycling in the Coastal Ocean: Continental Shelves as Sinks and near-Shore Ecosystems as Sources of Atmospheric CO2.” *Deep Sea Research Part II: Topical Studies in Oceanography* 56.8-10 (2009): 578–590.
13. Crosswell, Joseph R. et al. “Air-Water CO2 Fluxes in the Microtidal Neuse River Estuary, North Carolina.” *Journal of Geophysical Research* 117.C8 (2012): n. pag.

14. Cullison Gray, Sarah E. et al. “Applications of in Situ pH Measurements for Inorganic Carbon Calculations.” *Marine Chemistry* 125.1-4 (2011): 82–90.

15. Cussler, Edward Lansing. *Diffusion: Mass Transfer in Fluid Systems*. Cambridge university press, 2009. Print.

16. DeGrandpre, M. D. et al. “In Situ Measurements of Seawater pCO2.” *Limnology and Oceanography* (1995): 969–975. Print.

17. Edmond, John M. “High Precision Determination of Titration Alkalinity and Total Carbon Dioxide Content of Sea Water by Potentiometric Titration.” *Deep Sea Research and Oceanographic Abstracts* 17.4 (1970): 737–750..

18. Elliott, Michael, and Donald S. McLusky. “The Need for Definitions in Understanding Estuaries.” *Estuarine, Coastal and Shelf Science* 55.6 (2002): 815–827. Print.

19. Emerson, Steven, and John Hedges. *Chemical Oceanography and the Marine Carbon Cycle*. Cambridge University Press, 2008. Print.

20. Evans, Wiley, Burke Hales, and Peter G. Strutton. “pCO2 Distributions and Air–water CO2 Fluxes in the Columbia River Estuary.” *Estuarine, Coastal and Shelf Science* 117 (2013): 260–272.

21. Huyer, A. “Seasonal Cycle of Surface Ocean PCO2 on the Oregon Shelf.” *Journal of Geophysical Research* 116.C5 (2011): n. pag.

22. Feely, R. A. “Impact of Anthropogenic CO2 on the CaCO3 System in the Oceans.” *Science* 305.5682 (2004): 362–366.

23. Frankignoulle, Michel et al. “Carbon Dioxide Emission from European Estuaries.” *Science* 282.5388 (1998): 434–436. Print.

24. Goody, Richard. “Cross-Correlating Spectrometer.” *Journal of the Optical Society of America* 58.7 (1968): 900.

25. Green, Rebecca E. et al. “An Organic Carbon Budget for the Mississippi River Turbidity Plume and Plume Contributions to Air-Sea CO2 Fluxes and Bottom Water Hypoxia.” *Estuaries and Coasts* 29.4 (2006): 579–597.

26. Hales, Burke, David Chipman, and Taro Takahashi. “High-Frequency Measurement of Partial Pressure and Total Concentration of Carbon Dioxide in Seawater Using Microporous Hydrophobic Membrane Contractors.” (2004): n. pag. Print.

27. Hales, Burke, and Taro Takahashi. “The Pumping SeaSoar: A High-Resolution Seawater Sampling Platform.” *Journal of Atmospheric and Oceanic Technology* 19.7 (2002): 1096–1104. Print.

28. Hales, Burke, Taro Takahashi, and Leah Bandstra. “Atmospheric CO2 Uptake by a Coastal Upwelling System.” *Global Biogeochemical Cycles* 19.1 (2005): n/a–n/a.

29. Harris, Katherine E., Michael D. DeGrandpre, and Burke Hales. “Aragonite Saturation State Dynamics in a Coastal Upwelling Zone.” *Geophysical Research Letters* (2013): n/a–n/a.

30. Hatten, Jeff A., Miguel A. Goñi, and Robert A. Wheatcroft. “Chemical Characteristics of Particulate Organic Matter from a Small, Mountainous River System in the Oregon Coast Range, USA.” *Biogeochemistry* 107.1-3 (2010): 43–66.

31. Hickey, Barbara M., and Neil S. Banas. “Oceanography of the US Pacific Northwest Coastal Ocean and Estuaries with Application to Coastal Ecology.” *Estuaries and Coasts* 26.4 (2003): 1010–1031. Print.

32. Hunt, C. W., J. E. Salisbury, and D. Vandemark. “Contribution of Non-Carbonate Anions to Total Alkalinity and Overestimation of pCO_2 in New England and New Brunswick Rivers.” *Biogeosciences* 8.10 (2011): 3069–3076.

33. Huyer, Adriana. “Seasonal Variation in Temperature, Salinity, and Density over the Continental Shelf off Oregon.” (1977): n. pag. Print.

34. Huyer, A., E. J. C. Sobey, and R. L. Smith. “The Spring Transition in Currents over the Oregon Continental Shelf.” *Journal of Geophysical Research* 84.C11 (1979): 6995.

35. Jiang, Li-Qing, Wei-Jun Cai, and Yongchen Wang. “A Comparative Study of Carbon Dioxide Degassing in River-and Marine-Dominated Estuaries.” *Limnology and Oceanography* 53.6 (2008): 2603. Print.

36. Koseff, Jeffrey R. et al. “Coupled Effects of Vertical Mixing and Benthic Grazing on Phytoplankton Populations in Shallow, Turbid Estuaries.” *Journal of Marine Research* 51.4 (1993): 843–868.

37. Lebrato, Mario et al. “Global Contribution of Echinoderms to the Marine Carbon Cycle: $CaCO_3$ Budget and Benthic Compartments.” *Ecological Monographs* 80.3 (2010): 441–467.

38. Martz, Todd R., James G. Connery, and Kenneth S. Johnson. “Testing the Honeywell Durafet for Seawater pH Applications.” *Limnology and Oceanography: Methods* 8 (2010): 172–184.

39. McIntire, C. David, and W. Scott Overton. “Distributional Patterns in Assemblages of Attached Diatoms from Yaquina Estuary, Oregon.” *Ecology* (1971): 758–777. Print.

40. Millero, Frank J. et al. “Titration Alkalinity of Seawater.” *Marine Chemistry* 44.2 (1993): 153–165. Print.

41. Milliman, John D. “Production and Accumulation of Calcium Carbonate in the Ocean: Budget of a Nonsteady State.” *Global Biogeochemical Cycles* 7.4 (1993): 927–957.

42. Perkin, R., and E. Lewis. “The Practical Salinity Scale 1978: Fitting the Data.” *IEEE Journal of Oceanic Engineering* 5.1 (1980): 9–16.

43. Powell, Eric N., John N. Kraeuter, and Kathryn A. Ashton-Alcox. “How Long Does Oyster Shell Last on an Oyster Reef?” *Estuarine, Coastal and Shelf Science* 69.3-4 (2006): 531–542.

44. Pritchard, Donald W. “What Is an Estuary: Physical Viewpoint.” *Estuaries* 83 (1967): 3–5. Print.

45. Quinn, H. et al. “Susceptibility and Status of West Coast Estuaries to Nutrient Discharges: San Diego Bay to Puget Sound.” *Summary Report. NOAA/EPA. Rockville, MD* (1991): n. pag. Print.

46. Raymond, Peter A., James E. Bauer, and Jonathan J. Cole. “Atmospheric CO~ 2 Evasion, Dissolved Inorganic Carbon Production, and Net Heterotrophy in the York River Estuary.” *Limnology and Oceanography* 45.8 (2000): 1707–1717. Print.

47. Raymond, Peter A., and Jonathan J. Cole. “Gas Exchange in Rivers and Estuaries: Choosing a Gas Transfer Velocity.” *Estuaries* 24.2 (2001): 312–317.

48. Redfield, Alfred Clarence. *On the Proportions of Organic Derivatives in Sea Water and Their Relation to the Composition of Plankton*. University Press of Liverpool, 1934. Print.

49. Robbins, L. L. et al. “CO2calc—a User-Friendly Seawater Carbon Calculator for Windows, Max OS X, and iOS (iPhone).” *US Geological Survey Open-File Report* 1280.17 (2010): 2010. Print.

50. Roegner, G. Curtis, Charles Seaton, and António M. Baptista. “Climatic and Tidal Forcing of Hydrography and Chlorophyll Concentrations in the Columbia River Estuary.” *Estuaries and coasts* 34.2 (2011): 281–296. Print.

51. Sarmiento, Jorge L, and Nicolas Gruber. *Ocean Biogeochemical Dynamics*. Princeton: Princeton University Press, 2006. *Open WorldCat*. Web. 15 Aug. 2013.

52. Takahashi, Taro, R. F. Weiss, et al. “A Carbonate Chemistry Profile at the 1969 Geosecs Intercalibration Station in the Eastern Pacific Ocean.” *Journal of Geophysical Research* 75.36 (1970): 7648–7666.

53. Takahashi, Taro, Stewart C. Sutherland, Rik Wanninkhof, et al. “Climatological Mean and Decadal Change in Surface Ocean pCO2, and Net Sea–air CO2 Flux over the Global Oceans.” *Deep Sea Research Part II: Topical Studies in Oceanography* 56.8-10 (2009): 554–577.

54. Takahashi, Taro, Stewart C. Sutherland, Colm Sweeney, et al. “Global Sea–air CO2 Flux Based on Climatological Surface Ocean pCO2, and Seasonal Biological and Temperature Effects.” *Deep Sea Research Part II: Topical Studies in Oceanography* 49.9-10 (2002): 1601–1622.

55. Waldbusser, George G., Elizabeth L. Brunner, et al. “A Developmental and Energetic Basis Linking Larval Oyster Shell Formation to Acidification

Sensitivity: LARVAL SHELL AND ACIDIFICATION." *Geophysical Research Letters* 40.10 (2013): 2171–2176.

56. Waldbusser, George G., Erin P. Voigt, et al. "Biocalcification in the Eastern Oyster (Crassostrea Virginica) in Relation to Long-Term Trends in Chesapeake Bay pH." *Estuaries and Coasts* 34.2 (2011): 221–231. Print.
57. Wanninkhof, Rik. "Relationship between Wind Speed and Gas Exchange over the Ocean." *Journal of Geophysical Research* 97.C5 (1992): 7373.
58. Wei-Jun Cai et al. "Intertidal Marsh as a Source of Dissolved Inorganic Carbon and a Sink of Nitrate in the Satilla River-Estuarine Complex in the Southeastern US." *Limnology and Oceanography* 45.8 (2000): 1743–1752. Print.
59. Weiss, R_F. "Carbon Dioxide in Water and Seawater: The Solubility of a Non-Ideal Gas." *Marine Chemistry* 2.3 (1974): 203–215. Print.
60. Wilbur, K. M., and A. S. M. Saleuddin. "Shell Formation." *The mollusca* 4.Part 1 (1983): 235–287. Print.
61. Zeebe, Richard E. "History of Seawater Carbonate Chemistry, Atmospheric CO_2 , and Ocean Acidification." *Annual Review of Earth and Planetary Sciences* 40.1 (2012): 141–165.

APPENDICES

Appendix A: Required Parts List

Table A1: Required Parts List. This table lists part names for all components needed for construction of the ACDC instrument, along with quantity, vendor, and part number.

Category	Vendor	Part Name	Part Number	Quantity
Electronics	Arduino	Arduino Mega2560 Rev3	A000067	1
	Arduino	Arduino GSM Shield (integrated antenna)	A000043	1
	Adafruit	Adafruit Assembled Data Logging shield for Arduino	1141	1
	Adafruit	SD/MicroSD Memory Card (8 GB SDHC)	1294	1
	CO2meter	K-30 10,000ppm CO2 Sensor	SE-0018	1
	Digikey	Barometric Amplifiefd Pressure Sensor (BARO-A-4V-MINI)	442-1092-ND	1
	Adafruit	Waterproof DS18B20 Digital temperature sensor	381	1
	Adafruit	DS18B20 Digital temperature sensor	374	1
	McMaster-Carr	300 VAC/VDC Terminal Block, 6 Circuits, 3/8" Center-to-Center, 20 Amps	7527K46	1
	McMaster-Carr	Standard Ring Terminal, Noninsulated, 22-18 AWG, 5/16" Screw/Stud Size (100 ct bag)	7113K553	1
	Garmin	Garmin LVC 18x GPS	010-00321-31	1
	DigiKey	N-Channel Logic Level Power MOSFET 100 V, 12 A, 200 mΩ	RPF12N10L	1
	Bi-Mart	EverReady Gold C Alkaline Batteries	Energizer A93	4
Conductivity Board and Probe	NW MetaSystems Inc.	Conductivity Board	custom	1
	McMaster-Carr	3M Adhesive Cartridge, DP420 High Strength Epoxy, 1.25 Ounces, Off-White	7467A25	1
	McMaster-Carr	Solid Single-Conductor Wire, UL 1007/1569, 24 AWG, 300 VAC, Black	8073K611	n/a
Plumbing	Hargraves Fluidics	A.1F07N1.G05VDC CTS Diaphragm Pump, Coreless Motor	E-134-11-050	1
	Ballston Parker	Miniature Disposable Filter Units	9922-11	1
	McMaster-Carr	Push-to-Connect Tube Fitting for Air, Reducing Connector for 1/4" x 1/8" Tube OD (For Ballston Filter)	5779K352	2
	McMaster-Carr	Abrasion-Resistant White ETFE Tubing, .062" ID, 1/8" OD, .031" Wall, Semi-Clear White	5583K43	n/a
	McMaster-Carr	Push-to-Connect Tube Fitting for Air, Reducing Connector for 1/4" x 1/8" Tube OD	5779K352	2
	McMaster-Carr	Push-to-Connect Tube Fitting for Air, Reducing Inline Tee for 1/8" x 1/4" Tube OD	5779K665	1

Table A1: This table lists part names for all components needed for construction of the ACDC instrument, along with quantity, vendor, and part number (Continued).

Category	Vendor	Part Name	Part Number	Quantity
Pressure Housing	McMaster-Carr	Thick-Wall Dark Gray PVC Unthreaded Pipe Fitting, 6 Pipe Size x 11" OD, Easy Align Flange, Schedule 80	4881K241	1
	McMaster-Carr	Thick-Wall Dark Gray PVC Unthreaded Pipe Fitting, 6 Pipe Size x 11" OD, Cap Flange, Schedule 80	4881K972	1
	McMaster-Carr	Viton®Fluoroelastomer Gasket, Full Face-6" Pipe, 6-5/8" ID, 11" OD	9473K89	1
	McMaster-Carr	18-8 Stainless Steel Fully Threaded Hex Head Cap Screw, 1/2"-13 Thread, 4" Length	92240A728	8
	McMaster-Carr	18-8 Stainless Steel Nylon-Insert Hex Locknut, 1/2"-13 Thread Size, 3/4" Width, 19/32" Height	91831A137	8
	McMaster-Carr	18-8 Stainless Steel Large-Diameter Flat Washer, 1/2" Screw Size, 1-1/2" OD, .05"-.08" Thick	90313A117	8
	McMaster-Carr	Standard-Wall White PVC Pipe Fitting, 6 Pipe Size, Cap	4880K141	1
	Western Analytical	1/4” NPT M to 1/4-28 F Adapter, Red PEEK Includes (1) P-300/P-308 Fittings	U-500	2
	McMaster-Carr	Standard-Wall White PVC Unthreaded Pipe, 6 Pipe Size x 5' Length	48925K25	1
CO2 sensor housing	OSU Machine Shop	Aluminum K-30 enclosure	n/a (custom)	1
	McMaster-Carr	Nylon Liquid-Tight Cord Grip (NEMA 6), Straight Standard, PG7, .11"-.26" Cord Diameter	69915K147	1
	McMaster-Carr	Standard Straight Cord Grip, Nylon, 3/8" NPT Trade Size, .19"-.25" Cord Diameter	7529K152	2
Equilibrator	Perforated Tubes	4" perforated 316-SS tubes	n/a (custom)	1
	CelGard	Celgard 2400 Monolayer Polypropylene Membrane	n/a (custom)	n/a
	McMaster-Carr	Standard-Wall Type 316/316L Stainless Steel Thread Pipe Nipple, 3/4 Pipe Size x 2-1/2" Length	4548K194	1
Cellular Connectivity	AT&T	Cellular Plan	n/a	1

Appendix B: Arduino Mega 2560 R3 Code. Code developed for test deployments in Yaquina River Estuary and Oregon Near-Shore Fall 2013.

```
//code used for yaquina bay moored deployments
#include <OneWire.h>
#include <Metro.h>
#include <SD.h>
#include <Wire.h>
#include <RTClib.h>
#include <DallasTemperature.h>

#define pump 44
#define ONE_WIRE_BUS_PIN A0

//declarations for SD functionality
const int chipSelect = 10;
File dataFile;

//declarations for Real-Time Clock
RTC_DS1307 RTC;

//declarations for OneWire Protocol DS18B20
OneWire oneWire(ONE_WIRE_BUS_PIN);
DallasTemperature sensors(&oneWire);
DeviceAddress WTemp = { 0x28, 0x6D, 0xA5, 0x21, 0x05, 0x00, 0x00, 0xBC };
DeviceAddress ITemp = { 0x28, 0xE0, 0x36, 0x30, 0x05, 0x00, 0x00, 0x52 };

//declarations for K30 sensor
byte readCO2[] = {0xFE, 0X44, 0X00, 0X08, 0X02, 0X9F, 0X25}; //Command
packet to read Co2 (see app note)
byte response[] = {0,0,0,0,0,0,0}; //create an array to store the response
int valMultiplier = 1;

//declarations for GPS
char inChar;
int index;
String inData;
String gpsString;

//declarations for pump cycling
int pumpstate = LOW;
int pumpcycle = 0;
Metro pumpMetro = Metro(250);
```

```
void setup()
{
  Serial.begin(9600);
  Serial2.begin(4800);
  Serial3.begin(9600);
  pinMode(pump,OUTPUT);
  digitalWrite(pump,pumpstate);
  pinMode(10,OUTPUT);
  analogReference(DEFAULT);
  boolean notConnected = true;

  //initialize SD card and generate .txt file to store data
  Serial.print("Initializing SD card...");
  if (!SD.begin(chipSelect))
  {
    Serial.println("Card failed, or not present");
    while (1) ;
  }

  Serial.println("card initialized.");
  dataFile = SD.open("datalog.csv",FILE_WRITE);
  dataFile.println("Run Time,Time Stamp,Water Temp,Inner
Temp,pCO2,Pressure,Conductivity,Raw Cond,Pump State,GPS String");

  Wire.begin();
    if(!RTC.begin())
    {
      Serial.println("RTC failed");
    }
  sensors.begin();
  sensors.setResolution(WTemp, 12);
  sensors.setResolution(ITemp, 12);
}

void loop() {
  delay(60000);  //change to vary sampling frequency in milliseconds
//control the pump
    if (pumpMetro.check() == 1)
    {
      if (pumpstate == LOW)
      {
        pumpstate = HIGH;
        pumpMetro.interval(300000);
        pumpcycle ++;
      }
      else
```

```
    {
      pumpMetro.interval(600000);
      pumpstate = LOW;
    }
    digitalWrite (pump,pumpstate);
  }

 //get a timestamp stored to SD card for sample
  uint32_t m = millis();
  DateTime now;
  now = RTC.now();
  dataFile.print(m);
  dataFile.print(",");
  dataFile.print("");
  dataFile.print(now.month(), DEC);
  dataFile.print("/");
  dataFile.print(now.day(), DEC);
  dataFile.print("/");
  dataFile.print(now.year(), DEC);
  dataFile.print(" ");
  dataFile.print(now.hour(), DEC);
  dataFile.print(":");
  dataFile.print(now.minute(), DEC);
  dataFile.print(":");
  dataFile.print(now.second(), DEC);
  dataFile.print("");
  dataFile.print(",");

//read both DS18B20s, 1st is water temp, 2nd is internal temp
  sensors.requestTemperatures();
  printTemperature(WTemp);
  Serial.write(44);
  printTemperature(ITemp);
  Serial.write(44);

//read K-30 CO2 sensor
  sendRequest(readCO2);
  float rawCO2 = (getValue(response));
  float trueCO2 =  1.0434 * rawCO2 + 1.6197;
  Serial.print(trueCO2);
  Serial.write(44);

//Analog reads for pressure and conductivity
  int rawpressure = analogRead(A7);
  float pressure = ((rawpressure * (5.0 / 1023.0)) * 125 + 572.75);
  Serial.print(pressure);
```

```
 Serial.write(44);
 int rawcond = analogRead(A15);
 float mv_cond = rawcond * (5.0 / 1023.0);
 float inv_cond = (1 / mv_cond);
 float lin_cond = (inv_cond * 18147) + 4968.6;
 float conductivity = lin_cond;
 Serial.print(conductivity);
 Serial.write(44);
 Serial.print(rawcond);
 Serial.write(44);
 Serial.print(pumpstate);
 Serial.write(44);

//Store all environmentals and location to SD card
 dataFile.print(rawCO2);
 dataFile.print(", ");
 dataFile.print(trueCO2);
 dataFile.print(", ");
 dataFile.print(pressure);
 dataFile.print(", ");
 dataFile.print(conductivity);
 dataFile.print(", ");
 dataFile.print(rawcond);
 dataFile.print(", ");
 dataFile.print(pumpstate);
 dataFile.print(", ");

//Read from Garmin LVC 18x GPS string
 gpsString = "";
 delay(800);
 while(Serial2.available()>0)
 {
   inChar = Serial2.read();
   inData[index] = inChar;
   index++;
   gpsString += inChar;

   if (inChar == 87)
     {
       //36 = $, 42 = *, 87 = W
       index = 0;
       Serial.println(gpsString);
       dataFile.println(gpsString);
       //GPS UTC timestamp is 27 seconds slower than computer/my watch
     }
 }
```

```
  dataFile.flush();

}

void printTemperature(DeviceAddress deviceAddress)
{
  float tempC = sensors.getTempC(deviceAddress);
  if (tempC == -127.00)
    {
     Serial.print("T Error");
    }
  else
    {
     dataFile.print(tempC,2);
     dataFile.print(", ");
     Serial.print(tempC,2);
    }
}

void sendRequest(byte packet[])
{
  while(!Serial3.available()) //keep sending request until we start to get a
response
  {
   Serial3.write(readCO2,7);
   delay(50);
  }
    int timeout=0; //set a timeout counter
    while(Serial3.available() < 7 ) //Wait to get a 7 byte response
    {
      timeout++;
      if(timeout > 10) //if it takes to long there was probably an error
        {
         while(Serial3.available()) //flush whatever we have
         Serial3.read();
         break; //exit and try again
        }
       delay(50);
    }

  for (int i=0; i < 7; i++)
 {
 response[i] =  Serial3.read();
 }
}
unsigned long getValue(byte packet[])
```

```
{
 int high = packet[3]; //high byte for value is 4th byte in packet in the packet
 int low = packet[4]; //low byte for value is 5th byte in the packet
 unsigned long val = high*256 + low; //Combine high byte and low byte with this
formula to get value
 return val* valMultiplier;
}
```

Appendix C: Analyzed Discrete Bottle Data

Table C1: Analyzed Discrete Bottle Data. This table displays both the measured and calculated data for each discrete sample collected and discussed in this research.

Sample Date	Sample ID	*in situ* Temp	Analysis Temp	Salinity	PCO_2 @ Analysis Temp	TCO_2	T_{Alk}	TCO_2	*in situ* PCO_2	$CO_{2(aq)}$	HCO_3^-	CO_3^{2-}	pH	Ω-Calcite	Ω-Aragonite
		°C	°C	psu	µatm	µM	µeq kg^{-1}	µmol kg^{-1}	µatm	µmol kg^{-1}	µmol kg^{-1}	µmol kg^{-1}			
9-Jan-13	1	11.8	20.1	28.9	578.02	1860.19	1946.38	1823.55	413.04	17.70	1714.9	90.96	7.94	1.839	1.016
	2	11.8	19.7	29.8	558.07	1883.14	1976.11	1844.63	404.88	17.26	1731.4	95.97	7.95	1.920	1.061
	3	11.8	19.8	29.7	569.97	1876.70	1966.26	1838.50	412.09	17.58	1727.23	93.69	7.94	1.877	1.037
	4	11.8	20.0	29.8	579.59	1877.48	1966.07	1839.22	415.92	17.73	1728.38	93.11	7.94	1.863	1.030
	5	11.5	19.7	29.2	586.37	1844.43	1925.13	1807.52	420.74	18.17	1702.14	87.21	7.93	1.759	0.971
	6	11.5	19.3	28.6	582.93	1810.64	1885.57	1775.03	425.04	18.42	1673.92	82.70	7.92	1.683	0.929
	7	11.4	19.5	28.3	597.34	1795.07	1865.89	1760.24	430.64	18.76	1661.8	79.69	7.91	1.628	0.899
	8	11.5	19.8	28.0	595.13	1758.59	1827.82	1724.99	425.94	18.52	1629.03	77.44	7.91	1.593	0.879
	9	11.6	19.6	28.0	591.35	1757.96	1826.87	1724.28	428.30	18.57	1628.41	77.31	7.90	1.591	0.878
	10	11.6	19.4	28.7	573.88	1805.19	1882.52	1769.60	418.41	18.06	1667.63	83.90	7.92	1.707	0.943
	11	12.0	19.4	29.2	587.76	1843.88	1922.39	1806.85	435.81	18.52	1702.18	86.16	7.91	1.740	0.962
	12	12.2	19.8	29.0	594.44	1838.71	1917.15	1802.23	437.55	18.50	1697.84	85.89	7.91	1.741	0.962
	13	11.8	19.8	28.8	602.32	1829.45	1904.84	1793.42	436.22	18.70	1691.08	83.64	7.91	1.697	0.937
	14	11.7	19.4	28.5	602.45	1793.39	1862.69	1758.29	441.66	19.03	1660.36	78.91	7.90	1.611	0.889
	15	11.7	19.5	28.5	598.62	1778.32	1847.69	1743.56	437.18	18.84	1646.34	78.39	7.90	1.603	0.885
	16	11.7	19.8	28.2	608.12	1758.64	1825.36	1724.77	439.18	18.95	1629.71	76.11	7.89	1.563	0.863
	17	11.7	19.9	27.2	621.47	1689.50	1746.60	1658.24	447.76	19.43	1570.55	68.26	7.87	1.426	0.787

Table C1: Analyzed Discrete Bottle Data. This table displays both the measured and calculated data for each discrete sample collected and discussed in this research. (Continued)

Sample Date	Sample ID	*in situ* Temp	Analysis Temp	Salinity	PCO_2 @ Analysis Temp	TCO_2	T_{Alk}	TCO_2	*in situ* PCO_2	$CO_{2(aq)}$	HCO_3^-	CO_3^{2-}	pH	Ω-Calcite	Ω-Aragonite
		°C	°C	psu	µatm	µM	µeq kg^{-1}	µmol kg^{-1}	µatm	µmol kg^{-1}	µmol kg^{-1}	µmol kg^{-1}			
9-Jan-13 cont'd	18	11.4	19.6	26.2	620.22	1648.70	1699.85	1619.28	446.77	19.69	1536.07	63.52	7.87	1.344	0.741
	20	11.4	20.0	24.2	641.16	1543.23	1582.09	1518.11	455.98	20.33	1444.46	53.32	7.84	1.164	0.641
	21	11.5	20.3	24.2	655.46	1540.54	1578.23	1515.57	463.04	20.58	1442.39	52.60	7.83	1.149	0.633
	22	11.2	20.2	23.5	642.01	1502.92	1538.80	1479.30	449.76	20.26	1408.67	50.37	7.84	1.112	0.612
	23	11.2	20.1	23.2	657.30	1489.04	1520.95	1465.94	462.84	20.89	1397.13	47.91	7.82	1.062	0.585
7-Feb-13	1	9.3	21.1	31.6	489.73	1931.07	2066.77	1889.72	302.39	13.85	1751.38	124.49	8.12	2.951	1.603
	2	8.3	20.7	25.3	533.64	1567.83	1633.39	1541.31	322.58	15.85	1456.96	68.50	8.02	1.720	0.933
	3	8.4	20.7	24.5	528.49	1620.07	1690.23	1593.61	319.98	15.74	1504.92	72.95	8.04	1.847	1.002
	4	8.6	20.8	26.1	534.15	1623.59	1696.26	1595.21	325.42	15.75	1504.9	74.55	8.03	1.858	1.008
	5	8.7	20.8	26.8	535.35	1645.05	1720.85	1615.45	327.58	15.74	1522.56	77.15	8.03	1.910	1.036
	6	8.8	21.0	26.4	542.34	1636.30	1709.93	1607.43	330.70	15.87	1516	75.56	8.02	1.878	1.019
	7	8.8	20.8	27.1	524.24	1669.08	1750.62	1638.69	321.79	15.38	1541.94	81.37	8.04	2.009	1.090
	8	8.9	20.9	27.9	528.51	1726.03	1814.61	1693.63	324.34	15.38	1590.66	87.60	8.05	2.146	1.165
	9	9.0	21.0	28.7	530.05	1763.97	1858.55	1729.88	325.33	15.31	1621.98	92.59	8.05	2.252	1.223
	10	8.9	20.9	28.2	529.26	1730.92	1820.47	1698.06	324.86	15.38	1594.33	88.35	8.05	2.159	1.172
	11	9.0	21.0	28.9	537.15	1762.52	1855.46	1728.20	329.88	15.50	1621.14	91.56	8.05	2.223	1.207
	12	9.0	21.1	28.4	553.28	1766.05	1854.60	1732.35	338.56	15.96	1627.33	89.06	8.04	2.172	1.179
	13	9.0	20.9	28.2	565.60	1764.98	1848.69	1731.47	349.09	16.47	1628.8	86.21	8.03	2.106	1.144
	14	9.1	20.9	27.4	531.11	1676.67	1758.42	1645.81	329.04	15.54	1548.44	81.83	8.03	2.015	1.094

Table C1: Analyzed Discrete Bottle Data. This table displays both the measured and calculated data for each discrete sample collected and discussed in this research. (Continued)

Sample Date	Sample ID	*in situ* Temp	Analysis Temp	Salinity	PCO_2 @ Analysis Temp	TCO_2	T_{Alk}	TCO_2	*in situ* PCO_2	$CO_{2(aq)}$	HCO_3^-	CO_3^{2-}	pH	Ω-Calcite	Ω-Aragonite
		°C	°C	psu	µatm	µM	µeq kg^{-1}	µmol kg^{-1}	µatm	µmol kg^{-1}	µmol kg^{-1}	µmol kg^{-1}			
7-Feb-13 cont'd	15	9.1	21.0	26.6	525.14	1636.75	1714.92	1607.63	324.01	15.38	1513.97	78.28	8.03	1.942	1.055
	16	9.1	21.0	26.7	528.90	1638.38	1715.99	1609.11	326.42	15.48	1515.62	78.01	8.03	1.933	1.050
	17	9.1	21.1	26.3	539.21	1619.36	1692.41	1590.95	331.74	15.77	1500.49	74.69	8.02	1.858	1.009
	18	9.1	21.0	25.9	546.04	1586.10	1653.19	1558.69	337.65	16.09	1472.45	70.15	8.00	1.752	0.952
	19	9.2	21.0	25.1	543.26	1557.07	1620.68	1531.07	337.35	16.10	1447.76	67.21	8.00	1.692	0.919
	20	9.1	21.1	23.5	553.66	1473.27	1525.30	1450.44	341.77	16.51	1375.99	57.93	7.97	1.483	0.805
	21	9.1	21.1	23.9	547.69	1475.40	1529.38	1452.10	338.01	16.29	1376.73	59.07	7.98	1.506	0.818
	22	9.1	21.2	23.5	552.79	1438.11	1487.81	1415.86	340.27	16.44	1343.91	55.51	7.97	1.421	0.772
	23	9.2	21.2	23.3	552.69	1426.30	1474.75	1404.45	341.73	16.48	1333.5	54.47	7.96	1.398	0.759
	24	8.3	21.4	0.6	1557.40	335.18	277.59	335.73	1028.62	58.34	277.19	0.21	7.06	0.020	0.011
7-Mar-13	1	9.2	21.0	30.9	589.89	1912.11	2008.50	1872.09	372.75	17.20	1755.29	99.60	8.03	2.376	1.290
	2	8.6	20.3	25.9	571.84	1628.01	1687.62	1599.60	363.18	17.60	1514.58	67.42	7.98	1.683	0.913
	3	9.0	20.2	26.3	589.92	1658.39	1717.12	1628.92	382.58	18.25	1542.55	68.13	7.97	1.695	0.920
	4	8.8	20.2	26.7	583.22	1680.19	1742.83	1649.84	374.80	17.96	1560.82	71.06	7.98	1.761	0.956
	5	9.1	20.2	26.8	580.15	1670.49	1733.09	1640.19	377.66	17.90	1551.5	70.79	7.97	1.753	0.952
	6	9.3	20.4	26.8	579.91	1681.92	1746.61	1651.50	377.62	17.78	1561.35	72.37	7.98	1.792	0.974
	7	9.2	20.4	26.3	583.27	1659.98	1721.17	1630.56	378.40	17.93	1543.06	69.57	7.97	1.731	0.940
	8	9.3	20.0	26.3	577.97	1665.65	1726.45	1635.97	382.26	18.05	1548.27	69.65	7.97	1.733	0.942
	9	9.4	19.8	25.4	561.43	1596.10	1651.91	1568.64	376.05	17.79	1486.35	64.50	7.96	1.619	0.880

Table C1: Analyzed Discrete Bottle Data. This table displays both the measured and calculated data for each discrete sample collected and discussed in this research. (Continued)

Sample Date	Sample ID	*in situ* Temp	Analysis Temp	Salinity	PCO_2 @ Analysis Temp	TCO_2	T_{Alk}	TCO_2	*in situ* PCO_2	$CO_{2(aq)}$	HCO_3^-	CO_3^{2-}	pH	Ω-Calcite	Ω-Aragonite
		°C	°C	psu	µatm	µM	µeq kg^{-1}	µmol kg^{-1}	µatm	µmol kg^{-1}	µmol kg^{-1}	µmol kg^{-1}			
7-Mar-13 cont'd	10	9.3	19.8	24.9	558.94	1561.91	1614.57	1535.61	373.06	17.76	1456.29	61.56	7.96	1.553	0.844
	11	9.3	19.9	25.0	567.21	1569.86	1622.18	1543.34	377.20	17.95	1463.78	61.62	7.95	1.553	0.844
	12	9.5	20.2	24.0	567.79	1522.43	1570.63	1497.95	376.74	17.91	1422.31	57.74	7.95	1.471	0.799
	13	9.6	20.3	24.1	561.79	1531.31	1581.92	1506.60	372.70	17.65	1429.61	59.35	7.95	1.511	0.821
	14	9.7	19.9	24.1	553.54	1564.33	1617.47	1538.94	373.95	17.65	1459.38	61.92	7.96	1.576	0.857
	15	9.7	19.7	23.9	553.68	1503.69	1550.71	1479.43	377.63	17.84	1404.97	56.62	7.94	1.445	0.785
	16	9.7	19.7	22.8	558.88	1472.68	1514.81	1450.12	381.45	18.14	1379.05	52.93	7.93	1.367	0.743
	17	9.8	19.9	22.2	562.44	1428.21	1466.40	1407.03	383.09	18.22	1339.41	49.40	7.92	1.285	0.699
	18	9.8	20.2	21.1	587.75	1376.32	1406.65	1357.12	396.89	18.99	1294.49	43.63	7.89	1.150	0.625
	19	9.8	20.4	20.7	585.64	1369.15	1399.54	1350.52	392.45	18.82	1288.33	43.37	7.90	1.149	0.625
	20	9.8	20.1	20.1	590.40	1317.31	1341.92	1299.87	401.10	19.30	1241.61	38.96	7.87	1.040	0.565
	21	10.1	20.0	21.1	559.32	1383.03	1417.43	1363.67	384.64	18.22	1299.44	46.00	7.91	1.213	0.660
	22	8.5	20.2	0.7	1453.96	343.12	287.38	343.57	1002.61	56.43	286.9	0.24	7.08	0.022	0.012
14-Apr-13	15	10.3	20.4	23.8	514.85	1612.96	1693.52	1580.77	343.02	15.39	1486.13	79.24	8.00	1.917	1.043
	1	10.3	20.1	23.8	511.89	1615.22	1696.96	1581.81	345.32	15.42	1486.3	80.08	7.99	1.922	1.046
	2	10.3	20.3	24.6	517.43	1614.28	1695.27	1581.15	346.36	15.48	1486.1	79.58	7.99	1.912	1.041
	3	10.3	20.1	23.6	503.08	1615.27	1699.88	1581.57	339.28	15.13	1484.73	81.71	8.00	1.957	1.065
	4	10.4	19.7	23.6	510.89	1635.32	1719.79	1599.84	351.79	15.54	1501.72	82.58	7.99	1.960	1.067
	5	10.4	20.1	23.1	516.64	1628.18	1713.23	1592.70	350.36	15.46	1494.68	82.56	7.99	1.955	1.064

Table C1: Analyzed Discrete Bottle Data. This table displays both the measured and calculated data for each discrete sample collected and discussed in this research. (Continued)

Sample Date	Sample ID	*in situ* Temp	Analysis Temp	Salinity	PCO_2 @ Analysis Temp	TCO_2	T_{Alk}	TCO_2	*in situ* PCO_2	$CO_{2(aq)}$	HCO_3^-	CO_3^{2-}	pH	Ω-Calcite	Ω-Aragonite
		°C	°C	psu	µatm	µM	µeq kg^{-1}	µmol kg^{-1}	µatm	µmol kg^{-1}	µmol kg^{-1}	µmol kg^{-1}			
14-Apr-13 cont'd	14	10.4	19.8	24.9	497.00	1608.57	1696.19	1572.88	341.01	15.00	1474.57	83.30	7.99	1.964	1.069
	20	10.8	20.2	23.0	356.24	1481.79	1602.99	1449.81	243.42	10.61	1342.1	97.09	8.10	2.304	1.255
	6	10.7	20.3	24.3	470.73	1591.07	1687.94	1555.72	320.38	13.94	1454.02	87.76	8.01	2.065	1.125
	7	10.9	20.1	24.5	423.43	1537.03	1635.65	1505.46	292.01	12.80	1405.93	86.74	8.04	2.086	1.137
	19	10.6	20.0	25.8	473.64	1619.61	1713.17	1585.42	324.33	14.29	1484.05	87.07	8.02	2.080	1.132
	21	10.2	20.4	4.1	1478.03	377.02	320.90	377.55	1072.25	56.96	320.31	0.29	7.11	0.028	0.015
19-Apr-13	1	10.3	21.3	0.0	1305.71	390.29	342.14	391.10	926.07	49.20	341.68	0.22	7.30	0.055	0.030
	2	10.6	21.4	0.0	1292.15	399.66	352.22	400.50	922.99	48.54	351.72	0.24	7.32	0.060	0.032
	3	10.4	21.4	0.0	1299.93	396.19	348.43	397.02	922.34	48.83	347.95	0.23	7.31	0.058	0.032
	4	11.1	21.4	2.4	778.84	488.71	462.77	488.85	560.17	28.57	458.51	1.76	7.47	0.101	0.055
	5	11.6	21.4	14.3	717.21	1012.56	1008.57	1003.81	500.78	23.47	962.42	17.92	7.70	0.529	0.289
	6	11.5	21.5	14.3	672.29	1010.17	1009.83	1001.47	464.11	21.82	960.47	19.17	7.73	0.566	0.309
	7	11.1	21.5	10.1	567.11	789.90	785.76	785.56	388.04	18.94	754.47	12.15	7.73	0.401	0.219
	8	11.3	21.4	10.8	579.01	826.62	823.35	821.63	399.95	19.31	788.96	13.36	7.73	0.431	0.235
	9	11.3	21.5	16.4	521.16	1071.29	1091.04	1060.40	350.53	16.39	1014.47	29.53	7.86	0.837	0.456
	10	11.5	21.5	16.5	604.93	1102.49	1114.64	1091.20	412.77	19.17	1045.11	26.93	7.80	0.762	0.416
	11	11.1	21.4	9.9	554.48	790.22	786.69	785.98	380.31	18.58	755.07	12.32	7.74	0.409	0.223
	12	11.6	21.4	11.5	768.45	902.56	889.58	896.64	543.31	25.88	858.67	12.10	7.63	0.383	0.209
	13	10.9	21.0	7.9	627.20	705.45	692.64	702.65	440.35	21.91	673.09	7.66	7.65	0.275	0.150

Table C1: Analyzed Discrete Bottle Data. This table displays both the measured and calculated data for each discrete sample collected and discussed in this research. (Continued)

Sample Date	Sample ID	*in situ* Temp	Analysis Temp	Salinity	PCO_2 @ Analysis Temp	TCO_2	T_{Alk}	TCO_2	*in situ* PCO_2	$CO_{2(aq)}$	HCO_3^-	CO_3^{2-}	pH	Ω-Calcite	Ω-Aragonite
		°C	°C	psu	µatm	µM	µeq kg^{-1}	µmol kg^{-1}	µatm	µmol kg^{-1}	µmol kg^{-1}	µmol kg^{-1}			
19-Apr-13 cont'd	14	11.0	21.4	8.6	606.10	735.98	726.28	732.75	418.88	20.69	702.93	9.12	7.68	0.318	0.173
	15	11.5	21.4	10.3	638.73	822.52	814.58	817.86	447.65	21.54	784.63	11.69	7.68	0.384	0.209
	16	11.3	21.3	7.2	669.39	684.35	668.70	682.04	474.89	23.41	652.1	6.54	7.61	0.244	0.133
25-Apr-13	1	10.2	20.9	0.0	1542.87	454.83	397.08	455.74	1105.40	58.92	396.56	0.25	7.29	0.062	0.034
	2	8.9	21.1	33.0	1242.59	2176.68	2189.92	2127.85	788.46	36.31	2026.97	64.58	7.76	1.512	0.821
	3	8.1	21.0	32.6	1246.26	2168.57	2180.05	2120.50	768.56	36.45	2021.08	62.98	7.77	1.480	0.802
	4	8.9	21.0	33.6	1289.67	2190.45	2199.42	2140.31	822.67	37.75	2039.15	63.41	7.74	1.477	0.802
	5	8.6	21.1	32.3	1360.20	2198.83	2200.41	2150.63	855.93	39.98	2051.4	59.25	7.73	1.396	0.757
	6	9.3	21.1	33.8	1388.96	2217.21	2218.12	2166.18	899.73	40.69	2064.71	60.79	7.71	1.413	0.768
	7	8.8	20.7	33.5	1348.90	2203.24	2205.04	2152.79	868.18	40.00	2052.33	60.46	7.72	1.410	0.765
	8	13.3	20.8	10.6	874.16	894.03	872.52	888.64	685.89	31.07	847.78	9.78	7.54	0.320	0.175
	9	13.5	20.7	10.3	853.31	874.53	853.41	869.44	676.71	30.51	829.45	9.47	7.54	0.314	0.172
	10	13.5	20.7	7.4	866.06	724.57	698.64	721.92	691.36	31.69	684.7	5.53	7.47	0.206	0.113
	11	13.7	20.8	5.6	813.68	640.02	614.64	638.56	653.75	30.08	604.38	4.10	7.47	0.170	0.093
17-Oct-13	1	11.1	21.0	33.5	899.85	2092.35	2145.92	2044.60	620.39	26.49	1934.65	83.46	7.85	1.946	1.061
	2	12.1	20.7	33.9	877.37	2128.09	2187.09	2078.74	636.29	26.24	1964.05	88.44	7.85	2.055	1.122
	3	12.1	20.6	33.8	831.95	2142.81	2210.46	2093.23	604.70	24.96	1974.42	93.85	7.87	2.182	1.192
	4	11.6	20.6	33.9	816.63	2134.00	2204.02	2084.46	581.54	24.37	1965.34	94.75	7.89	2.201	1.201
	5	11.7	20.6	33.9	860.19	2165.77	2230.24	2115.50	615.42	25.71	1996.94	92.85	7.87	2.157	1.177

Table C1: Analyzed Discrete Bottle Data. This table displays both the measured and calculated data for each discrete sample collected and discussed in this research. (Continued)

Sample Date	Sample ID	*in situ* Temp	Analysis Temp	Salinity	PCO_2 @ Analysis Temp	TCO_2	T_{Alk}	TCO_2	*in situ* PCO_2	$CO_{2(aq)}$	HCO_3^-	CO_3^{2-}	pH	Ω-Calcite	Ω-Aragonite
		°C	°C	psu	µatm	µM	µeq kg^{-1}	µmol kg^{-1}	µatm	µmol kg^{-1}	µmol kg^{-1}	µmol kg^{-1}			
17-Oct-13 cont'd	6	11.6	20.9	33.2	843.43	2168.61	2237.08	2119.54	593.65	24.98	1999.82	94.74	7.89	2.215	1.208
	7	12.6	20.9	32.0	847.77	2075.90	2133.94	2030.74	622.25	25.53	1920.1	85.10	7.85	2.012	1.100
	8	12.2	20.7	32.6	836.31	2101.43	2163.33	2054.68	608.24	25.19	1941.06	88.43	7.86	2.079	1.136
	9	12.2	20.8	32.4	821.97	2094.31	2158.51	2048.08	595.38	24.69	1934.06	89.34	7.87	2.104	1.149
	10	12.0	20.7	32.7	823.34	2101.52	2165.97	2054.63	593.84	24.74	1940.03	89.85	7.87	2.110	1.152
	11	12.2	20.8	33.2	759.34	2107.03	2186.22	2059.30	549.17	22.67	1937.84	98.79	7.91	2.310	1.262
	12	12.5	20.9	33.4	704.57	2110.07	2202.96	2062.02	513.22	20.96	1933.92	107.14	7.94	2.501	1.367
	13	12.4	21.0	33.1	704.29	2088.57	2179.40	2041.51	509.07	20.89	1915.74	104.88	7.94	2.455	1.341
	14	12.3	20.8	32.9	823.17	2113.49	2179.95	2066.07	598.60	24.67	1949.78	91.62	7.87	2.148	1.173
	15	12.5	21.0	32.3	842.87	2103.54	2165.77	2057.37	613.50	25.21	1943.59	88.57	7.86	2.088	1.141
	16	12.4	20.8	31.8	859.15	2088.43	2144.57	2043.24	627.86	25.96	1932.91	84.38	7.85	1.999	1.092
	17	12.5	20.8	31.3	870.02	2068.97	2121.01	2024.96	638.74	26.40	1917.36	81.20	7.84	1.932	1.056
	18	11.9	20.9	0.0	1773.26	470.37	403.83	471.30	1344.59	67.70	403.37	0.23	7.22	0.057	0.031

Table C1: Analyzed Discrete Bottle Data. This table displays both the measured and calculated data for each discrete sample collected and discussed in this research. (Continued)

Sample Date	Sample ID	*in situ* Temp	Analysis Temp	Salinity	PCO_2 @ Analysis Temp	TCO_2	T_{Alk}	TCO_2	*in situ* PCO_2	$CO_{2(aq)}$	HCO_3^-	CO_3^{2-}	pH	Ω-Calcite	Ω-Aragonite
		°C	°C	psu	µatm	µM	µeq kg^{-1}	µmol kg^{-1}	µatm	µmol kg^{-1}	µmol kg^{-1}	µmol kg^{-1}			
29-Oct-13	1	9.1	22.0	34.6	1272.03	2195.97	2213.72	2144.68	787.89	35.70	2040.64	68.34	7.76	1.578	0.857
	2	9.1	22.5	31.9	1274.64	2062.35	2072.45	2018.50	777.64	35.79	1924.44	58.26	7.75	1.377	0.748
	3	9.7	22.0	31.5	1286.40	2055.12	2060.81	2011.74	819.39	37.05	1918.64	56.05	7.72	1.330	0.723
	5	10.0	21.7	31.2	1217.65	2028.15	2037.60	1985.62	792.05	35.52	1893.21	56.90	7.73	1.354	0.736
	4	9.2	21.8	30.7	1229.04	2031.85	2040.40	1990.04	771.52	35.64	1898.33	56.07	7.75	1.340	0.728
	6	9.2	21.8	31.0	1310.67	2056.03	2058.04	2013.27	825.02	38.05	1921.21	54.02	7.72	1.287	0.699
	7	10.0	21.8	31.5	1215.68	2042.15	2053.31	1998.94	787.50	35.26	1905.38	58.30	7.74	1.383	0.753
	8	9.9	22.0	32.2	1214.74	2047.65	2060.87	2003.38	778.03	34.81	1908.8	59.78	7.74	1.410	0.767
	9	10.1	22.0	31.9	1172.40	2058.63	2076.77	2014.58	755.33	33.63	1918.55	62.40	7.76	1.475	0.803
	10	10.0	21.8	31.4	1139.68	2051.81	2071.69	2008.55	735.78	32.96	1912.82	62.77	7.77	1.491	0.811
	11	10.2	21.8	31.7	1132.23	2041.81	2062.27	1998.31	736.99	32.74	1902.63	62.94	7.77	1.491	0.811
	12	10.5	21.6	31.7	1144.31	2049.82	2068.32	2006.04	759.66	33.42	1910.24	62.39	7.76	1.478	0.805
	13	10.7	21.8	31.7	1128.62	2039.14	2059.86	1995.70	749.46	32.75	1899.82	63.12	7.76	1.495	0.815
	14	10.5	21.7	32.2	1158.09	2054.12	2072.35	2009.56	766.40	33.61	1913.29	62.66	7.75	1.478	0.805
	15	10.6	21.8	32.1	1155.47	2043.42	2061.75	1999.29	764.97	33.46	1903.54	62.29	7.75	1.470	0.801
	16	10.4	21.7	32.3	1211.69	2065.27	2078.33	2020.31	800.03	35.19	1924.55	60.57	7.74	1.427	0.777
	17	10.6	21.7	32.5	1273.99	2067.67	2074.59	2022.37	849.80	37.09	1927.34	57.94	7.71	1.363	0.742
	18	10.6	21.6	33.2	1275.60	2061.39	2067.94	2015.12	854.40	37.14	1919.97	58.00	7.71	1.356	0.738
	19	12.0	21.6	18.4	1577.30	1322.67	1277.72	1307.30	1152.58	52.09	1240.72	14.49	7.43	0.398	0.217

Table C1: Analyzed Discrete Bottle Data. This table displays both the measured and calculated data for each discrete sample collected and discussed in this research. (Continued)

Sample Date	Sample ID	*in situ* Temp	Analysis Temp	Salinity	PCO_2 @ Analysis Temp	TCO_2	T_{Alk}	TCO_2	*in situ* PCO_2	$CO_{2(aq)}$	HCO_3^-	CO_3^{2-}	pH	Ω-Calcite	Ω-Aragonite
		°C	°C	psu	µatm	µM	µeq kg^{-1}	µmol kg^{-1}	µatm	µmol kg^{-1}	µmol kg^{-1}	µmol kg^{-1}			
1-Nov-13	1	9.6	21.8	33.7	1045.76	2140.02	2180.06	2091.32	660.82	29.60	1984.37	77.34	7.83	1.800	0.978
	2	9.8	21.6	33.6	1087.88	2146.33	2179.80	2097.53	699.25	31.14	1992.21	74.19	7.81	1.728	0.940
	3	9.9	21.7	33.8	1103.10	2140.19	2172.12	2091.27	709.85	31.47	1986.51	73.30	7.80	1.704	0.927
	4	9.8	21.6	33.8	1034.39	2142.73	2183.52	2093.70	663.68	29.52	1986.17	78.01	7.83	1.814	0.986
	24	10.0	21.5	33.8	1042.94	2152.82	2192.51	2103.50	677.21	29.92	1995.68	77.90	7.82	1.811	0.985
	5	9.8	21.6	33.6	1000.95	2144.27	2189.70	2095.52	641.31	28.56	1986.53	80.43	7.84	1.873	1.019
	6	9.9	21.5	33.7	986.80	2142.42	2189.37	2093.50	636.98	28.25	1983.94	81.30	7.85	1.892	1.029
	7	10.1	21.7	33.3	1108.76	2145.58	2176.48	2097.31	719.18	31.76	1992.83	72.72	7.80	1.698	0.924
	8	10.0	21.6	33.5	986.88	2151.20	2199.07	2102.44	637.02	28.19	1992.23	82.01	7.85	1.912	1.040
	9	10.5	21.5	32.4	1181.24	2122.19	2140.82	2075.73	786.77	34.47	1975.91	65.35	7.76	1.538	0.838
	10	10.6	21.7	32.3	1172.90	2131.78	2152.89	2085.37	778.06	34.00	1984.54	66.83	7.76	1.575	0.858
	11	10.3	21.7	33.8	1079.85	2145.70	2181.05	2096.66	705.52	30.86	1990.41	75.39	7.80	1.753	0.954
	12	10.7	21.6	33.5	1094.92	2135.09	2166.79	2086.70	730.24	31.58	1982.02	73.10	7.79	1.704	0.928
	13	10.7	21.8	33.5	1042.53	2128.97	2168.42	2080.82	688.95	29.80	1974.16	76.86	7.81	1.792	0.976
	14	10.5	21.7	34.4	951.82	2134.67	2188.81	2084.95	624.47	27.05	1972.44	85.47	7.85	1.976	1.076
	15	10.7	21.6	34.3	980.69	2120.45	2168.25	2071.16	651.95	28.07	1961.57	81.52	7.83	1.887	1.028
	16	10.8	21.6	33.2	974.16	2119.70	2166.73	2072.12	649.78	28.06	1963.56	80.50	7.84	1.882	1.025
	17	10.3	21.6	33.3	1102.51	2141.60	2172.49	2093.38	723.52	31.74	1988.97	72.66	7.79	1.697	0.924
	18	10.3	21.4	32.6	1144.06	2139.63	2163.28	2092.42	757.40	33.36	1990.51	68.54	7.77	1.611	0.877

Table C1: Analyzed Discrete Bottle Data. This table displays both the measured and calculated data for each discrete sample collected and discussed in this research. (Continued)

Sample Date	Sample ID	*in situ* Temp	Analysis Temp	Salinity	PCO_2 @ Analysis Temp	TCO_2	T_{Alk}	TCO_2	*in situ* PCO_2	$CO_{2(aq)}$	HCO_3^-	CO_3^{2-}	pH	Ω-Calcite	Ω-Aragonite
		°C	°C	psu	µatm	µM	µeq kg^{-1}	µmol kg^{-1}	µatm	µmol kg^{-1}	µmol kg^{-1}	µmol kg^{-1}			
24-Nov-13	1	10.2	20.2	32.5	658.92	2062.15	2154.55	2016.17	447.97	19.81	1892.31	104.05	7.98	2.447	1.332
	2	10.3	20.2	33.6	639.80	2073.11	2174.15	2025.23	436.77	19.13	1896.05	110.06	7.99	2.563	1.395
	3	10.3	20.3	33.5	640.79	2076.50	2178.09	2028.74	435.71	19.09	1899.19	110.46	7.99	2.575	1.401
	4	10.5	20.4	32.6	634.83	2078.08	2179.94	2031.70	433.23	18.96	1902.29	110.44	8.00	2.595	1.413
	5	10.4	20.4	33.1	631.07	2079.31	2183.55	2032.15	428.96	18.78	1901.32	112.05	8.00	2.621	1.427
	6	10.5	20.4	33.0	628.21	2072.27	2176.29	2025.42	428.80	18.72	1895.07	111.63	8.00	2.614	1.423
	7	10.1	20.1	32.8	611.04	2049.43	2153.13	2003.24	414.86	18.37	1874.46	110.41	8.01	2.590	1.409
	8	10.2	20.3	33.1	613.09	2064.29	2171.18	2017.41	414.78	18.28	1886.13	113.00	8.01	2.644	1.439
	9	10.3	20.3	33.1	608.07	2059.45	2167.24	2012.69	413.08	18.14	1881.16	113.38	8.01	2.653	1.444
	10	10.4	20.4	32.9	614.03	2060.60	2167.04	2014.16	417.27	18.29	1883.31	112.56	8.01	2.638	1.436
	11	10.4	20.4	33.0	615.05	2055.52	2161.37	2009.04	418.04	18.31	1878.7	112.03	8.01	2.623	1.428
	12	10.4	20.4	33.2	608.04	2063.12	2172.28	2016.17	413.20	18.08	1883.68	114.41	8.01	2.674	1.456
	13	10.5	20.2	32.9	602.73	2074.90	2184.68	2028.03	414.27	18.10	1894.66	115.27	8.02	2.702	1.471
	14	10.4	20.3	32.9	606.82	2079.58	2189.42	2032.66	413.73	18.13	1899.09	115.43	8.02	2.705	1.473

Table C1: Analyzed Discrete Bottle Data. This table displays both the measured and calculated data for each discrete sample collected and discussed in this research. (Continued)

Sample Date	Sample ID	*in situ* Temp	Analysis Temp	Salinity	PCO_2 @ Analysis Temp	TCO_2	T_{Alk}	TCO_2	*in situ* PCO_2	$CO_{2(aq)}$	HCO_3^-	CO_3^{2-}	pH	Ω-Calcite	Ω-Aragonite
		°C	°C	psu	µatm	µM	µeq kg^{-1}	µmol kg^{-1}	µatm	µmol kg^{-1}	µmol kg^{-1}	µmol kg^{-1}			
18-Dec-13	3	6.0	0.6	5.5	747.77	659.55	604.71	656.69	919.41	54.99	599.71	2.00	7.29	0.081	0.044
	6	6.1	0.7	6.5	718.13	717.35	665.40	713.67	883.62	52.35	658.62	2.70	7.33	0.102	0.055
	8	6.2	0.7	6.7	727.21	723.03	670.41	719.21	898.11	52.95	663.51	2.74	7.33	0.103	0.055
	10	6.1	0.5	4.4	744.34	619.81	564.73	617.68	921.85	55.29	560.78	1.61	7.28	0.071	0.038
	12	6.3	0.5	6.5	718.10	713.09	660.68	709.44	897.11	52.77	654.02	2.65	7.32	0.100	0.054
	14	6.3	0.7	6.4	728.11	700.80	647.99	697.26	902.16	53.10	641.65	2.52	7.31	0.096	0.052
	17	6.3	0.7	6.5	735.79	710.45	657.09	706.81	911.70	53.63	650.6	2.58	7.31	0.098	0.053
	1	6.0	12.7	6.1	1078.58	652.57	602.28	649.87	855.95	51.01	596.64	2.22	7.31	0.086	0.046
	2	6.0	12.8	6.2	1071.98	659.12	609.42	656.36	847.77	50.50	603.56	2.31	7.32	0.089	0.048
	4	6.0	12.7	7.8	989.17	718.25	673.32	714.35	783.90	46.25	664.78	3.32	7.37	0.118	0.063
	5	6.1	13.2	7.1	912.78	684.23	643.83	680.93	713.94	42.15	635.56	3.22	7.40	0.118	0.064
	7	6.1	13.4	7.7	1041.90	712.84	666.40	709.10	810.00	47.65	658.3	3.15	7.36	0.112	0.061
	9	6.1	13.0	5.4	1090.62	616.93	566.29	614.74	860.49	51.31	561.56	1.87	7.29	0.076	0.041
	11	6.3	14.3	7.3	1072.77	710.74	664.34	707.32	815.82	47.76	656.49	3.07	7.36	0.112	0.060
	13	6.3	14.3	7.3	1091.43	703.21	655.82	699.83	830.20	48.60	648.28	2.94	7.34	0.107	0.058
	15	6.3	13.7	6.2	1109.46	661.74	611.86	659.05	861.39	50.76	605.98	2.32	7.31	0.090	0.048
	16	6.2	14.1	7.3	1050.96	714.99	669.35	711.53	801.35	47.08	661.29	3.16	7.37	0.115	0.062